Master Thesis

Segmentation of bone structures in Magnetic Resonance Images (MRI) for human hand skeletal kinematics modelling

Alexandru Rusu

DLR

Institut für Robotik und Mechatronik	BJ.: 2011
	IB.Nr.: 572-11-22

MASTERARBEIT

SEGMENTATION OF BONE STRUCTURES IN MAGNETIC RESONANCE IMAGES (MRI) FOR HUMAN HAND SKELETAL KINEMATICS MODELLING

Freigabe:	Der Bearbeiter:	Unterschriften
	Alexandru Rusu	i. A. Georg Stillfried
	Betreuer:	
	Georg Stillfried	Georg Stillfried
	Der Institutsdirektor	
	Prof. Dr. G. Hirzinger	

Dieser Bericht enthält 53 Seiten, 27 Abbildungen und 1 Tabelle

Ort: Oberpfaffenhofen	Datum: 25.01.2012	Bearbeiter:	Zeichen:

Segmentation of bone structures in Magnetic Resonance Images (MRI) for human hand skeletal kinematics modelling

Alexandru Rusu

Supervised by:
Dipl. Ing. Georg Stillfried
Institute of Robotics and Mechatronics
German Aerospace Center (DLR)
Oberpfaffenhofen
82234 Wessling, Germany

A Thesis Submitted for the Degree of
MSc Erasmus Mundus in Vision and Robotics (VIBOT)

· 2011 ·

Contents

List of Figures

List of Tables

Chapter 1

Introduction

The human hand is one of the most complicated biomechanical structures of the human body. It consists of bones, articulations, muscles, tendons, fat and skin. During the evolution, the human hand expanded its functionalities, mainly related to the physical exploitation of the environment. Due to its complex and delicate structure, it is able to carry out very accurate grasping tasks (like picking up a needle) but also to accomplish activities which require gross power skills (such as weight lifting). All these capabilities led to a high interest of roboticists in designing and building robotic hands, which are able to copy the human hand kinematics and dynamic characteristics.

A very elaborate and accurate model of the human hand can be applied in different domains: from prostheses (where the human-like motion is of very high interest for cosmetic reasons) to telemanipulation and service robotics (where the accuracy of the interaction with the environment is important). Another skill which is widely studied in the literature is related to the grasping accuracies. For an accurate modelling of the hand kinematics medical imaging techniques are employed, and several steps have to be undertaken:

- Data acquisition: Firstly MR 3D image volumes have to be recorded in different postures. The postures have to be as diversified as possible, so all the kinematic range can be characterized.
- Segmentation: For each posture, extract the information from the 3D MR volume which belongs to each bone structure.
- Pose estimation: Estimate the position and orientation of each bone with respect to a reference coordinate system.
- Define the joint axes and identify the hand model: Estimate the type, position and

orientation of the joint axes, which optimally integrate the bone structures and derive the kinematic chain based on their combination taking also into account the conciliation between complexity and accuracy.

In this thesis, the analysis of the human hand structure is made from the medical image segmentation point of view. Medical image segmentation refers to the extraction of the anatomical structures of interest from digital images. The purpose is to accurately extract the bone structure of the human hand in different postures in order to be able to model a precise kinematic model.

Image segmentation is a fundamental field in computer vision and many methods have been developed with a view to deal with the limitations of the real-world studied datasets and the varied requirements. Image segmentation algorithms can be easily classified in three groups: for manual, semi-automatic and automatic segmentation. Manual segmentation is usually the most precise technique, but it entails domain experts and it is very laborious and time consuming. Also, the results of the manual segmentation procedures are affected by the subjective analysis of the expert in charge. While semi-automatic segmentation algorithms need initialization (some parameters or even regions of interest for the structures to be segmented), the automatic algorithms have to extract the structures of interest independently, without any input from the user. Besides, the results of the segmentation algorithms are affected by image artefacts like noise, intensity inhomogeneities and low contrast between distinct regions. The problems medical segmentation algorithms have to deal with are detailed in section 2 and a general introduction to the segmentation techniques applied in medical images with their advantages and disadvantages is presented in Section 3.

1.1 Motivation

Most of the kinematic data used for hand modelling have been acquired using optical surface markers. These surface markers are fastened to the skin and traced by optical measuring systems (eg. Vicon). The estimated position and orientation of the markers in the calibrated space, incorporated in a skeletal model, can help developing a good representation of the hand kinematics. However , this approach experiences several drawbacks, one of the most important ones being called the skin movement artefacts. It refers to the fact that the movement of optical markers cannot totally and accurately describe the bone motion, mainly because of the unmodellable and unstable movement of the soft tissue (skin).

This is the reason for which more accurate hand models are needed, which take into consideration all the internal finger movements. This motivation leaded to conduct measurements on hand cadavers, but it proved to be unreliable because of the rigidity of muscles or tendons,

which would lead to errors in the kinematics representation. In order to handle the quality requirements for the design of an accurate hand model, modern *in vivo* imaging techniques are applied to record a high number of hand postures. The advantage of taking *in vivo* measurements on awake subjects is that it offers the opportunity to study in detail the movement of the bones and the behaviour of the soft tissues. Two medical imaging techniques offer high resolution data essential for this type of analysis: MRI and CT.

Computed tomography (CT) is a non-invasive imaging technique, widely available, and useful for the rapid visualization and localization of anatomic structures. The principle behind CT scanning is that of conventional X-ray imaging, with ionizing radiation being emitted in rotatory motion around the patient. This radiation passes through the tissue in multiple directions, X-ray photon detectors measuring the degree of attenuation of the exiting radiation. Then, the obtained data are integrated to produce images of scanned anatomical structure in 2D or 3D representation. This technique is more suitable for bone imaging, but because of the radiation exposure it has been discarded.

Magnetic resonance imaging (MRI), on the other hand, is also a non-invasive imaging technique, which provides greater contrast in soft tissues without exposure to ionizing radiation. It is based on the application of a powerful steady magnetic field, lining up the hydrogen atoms in the tissue being imaged, and additional radio frequency fields, used to alter the alignment of the magnetization, and to produce an effect detectable by the scanner. It is also able to carry out 3D imaging of biological structures, but slower and at a lower resolution comparing with CT.

In spite of the disadvantages it has with respect to CT imaging, MRI imaging is chosen here, taking into account that no ionizing radiation is involved, which could give high risks for the health of the subjects to be imaged, due to the large acquisition times.

1.2 Objectives

Around 50 hand postures from 3 different subjects were imaged using MRI sequences. The goal of this thesis is to perform segmentation algorithms for the extraction of bone structures from the 3D medical image volumes. It is of very high interest to segment either a fixed structure for each bone which is easy to reproduce in all the other datasets, or to segment accurately each hand posture. This is needed for the next step of the hand modelling, the pose estimation and registration between two different poses. Usually the general segmentation algorithms are addressing a 2D problem and a special interest on extending their capabilities to 3D datasets has been confirmed.

Segmenting bone regions in MRI data volumes is not a straightforward task, and it is going

to be proved further on. The bone can be divided in two sections: the *cancellous bone*, the interior part, generally consisting of fat, which is represented by bright areas in MR images and the *cortical bone*, the exterior calcified section of the bone which can be identified as dark regions in the MR datasets (because of the lack of fat or water protons). Therefore the algorithm focuses on the segmentation of the boundary between high intensity signal inside the *cancellous bone* and the *cortical bone*. Around the bones there are additional soft tissues (like tendons, muscles, fat) with similar intensities to those of the internal parts of the bone, which make the segmentation process very difficult. This is the reason for which in some cases it is delicate to accurately decide on the boundary of the bone. Figure 1.1 presents the introduced notions for a better understanding of the problem.

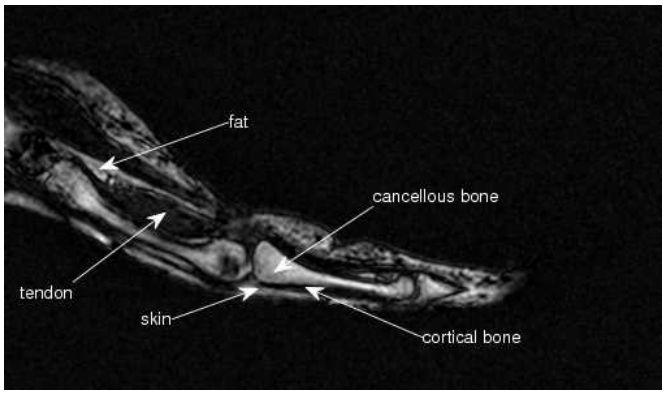

Figure 1.1: Example of an MRI image showing the type of tissues in the hand

Sumarizing, a segmentation algorithm has to be developed for the accurate segmentation of bone structures in 3D MRI dataset which should be able to overcome the shortcomings of the used imaging techniques. Some of the difficulties are related to noise, intensity inhomogeneities and partial volume effects. Section 2 gives an introduction on the MRI techniques and provides details on the aformentioned challenges. Section 3 presents an overview of image segmentation techniques applied in medical image analysis discussing their advantages and disadvantages and referring to their applications in the field of study. The Level Set methods are introduced in the next chapter, as they are the proposed method to accomplish the segmentation task and their results are assessed. The segmentation algorithm has to be as independent as possible, trying to minimize the manual interaction of the user. This is the reason for which it comes in the format of a stand alone application which is described in Section 5 and the obtained results are evaluated using some predefined quality measures.

Chapter 2

Problem definition

2.1 Magnetic Resonance Imaging

MRI is a non-invasive radiology technique generating anatomical and functional images of the body, and particularly useful for neurological, oncological, cardiovascular, muscular and skeletal imaging. Images can be obtained in any orientation, rapidly, non-invasively, and without exposure to ionizing radiation. MRI technology is based on the application of a powerful steady magnetic field, lining up the hydrogen atoms in the tissue being imaged, and additional radio frequency fields, used to alter the alignment of the magnetization, and to produce an effect detectable by the scanner. It allows for the variation of parameters such as repetition time (TR - the time between two consecutive excitation pulses) and echo time (TE - the time between the excitation pulse and the recording of the magnetization value).

Many pulse sequences are available in MR imaging techniques which leads to an optimization problem. Depending on the anatomy of the structures of interest, the optimal pulse sequence has to be chosen in order to be able to optimally distinguish the tissues of interest and to undertake the segmentation procedure. For instance, MR imaging of brain tissues requires a specific setup in comparison to bone analysis. Despite the non-ionizing radiation characteristics, MR imaging experiences different imaging artefacts which generate difficulties for the segmentation techniques having considerable effects on their performances [51]. Some of the drawbacks of this imaging technique are: noise, low contrast between certain tissues, partial volume effects, and intensity inhomogeneities. These shortcomings shall be discussed further on.

2.1.1 Noise in MR Imaging

In magnetic resonance imaging (MRI) there is a trade off between signal-to-noise ratio (SNR), acquisition time and spatial resolution. The SNR is relatively high in most MRI applications, and this is accomplished implicitly and explicitly by averaging. The MRI data acquisition process can be affected by two averaging techniques:

- Spatial volume averaging is required due to the discrete nature of the acquisition process;
- In the case of some applications, the signal for the same k-space location is acquired several times and averaged in order to reduce noise.

The two averaging methods are interconnected. When a higher sampling rate of the frequency domain is used, higher resolution images are obtained. However, in order to receive a desired SNR at high spatial resolution a longer acquisition time is required, as additional time for averaging is necessary. Conversely, the acquisition time, with the subsequent SNR and the imaging resolution, are practically limited by the patient comfort and the system throughput. Consequently, high SNR MRI images can be acquired at the expense of constrained temporal or spatial resolution. Also, high resolution MRI imaging is achievable at a cost of lower SNR or longer acquisition times.

Another important source of noise in MRI imaging is thermal noise in the human body. Common MRI imaging involves sampling in the frequency domain (also called *"k-space"*), and the MRI image is computed using the Inverse Discrete Fourier Transform. Signal measurements have components in both real and imaginary channels and each channel is affected by additive white Gaussian noise. Thus, the complex reconstructed signal includes a complex white additive Gaussian noise. Due to phase errors, usually the magnitude of the MRI signal is used for the MRI image reconstruction. The magnitude of the MRI signal is real-valued and is used for the image processing tasks, as well for visual inspection. Considering the received MRI signal $y[m,n]$ in eq. 2.1, where $s[m,n]$ is the complex signal of interest and $n[m,n]$ is the additive complex Gaussian noise, the magnitude image at the pixel position m,n is computed using eq. 2.2, where θ represents the phase error of the received MRI signal and n_r and n_i are white Gaussian noises.

$$y[m,n] = s[m,n] + n[m,n] \tag{2.1}$$

$$x[m,n] = |y[m,n]| = \sqrt{(s[m,m]\cos\theta + n_r[m,n])^2 + (s[m,n]\sin\theta + n_i[m,n])^2} \tag{2.2}$$

The way the magnitude MRI image is reconstructed results in a Rician distribution of the noise. The main remark is that the Rician noise is signal-dependent, separating the signal from noise being a very difficult task. In high intensity areas of the magnitude image, Rician distribution can be approximated to a Gaussian distribution, and in low intensity regions it can be estimated as a Rayleigh distribution. A practical effect is a reduced contrast of the MRI image, as the noise increases the mean intensity values of the pixels in low intensity regions.

Figure 2.1 displays a comparison between the effect of Rician noise and Gaussian noise added to a MRI image. It can be also noted that the adding of Gaussian noise produced some negative data.

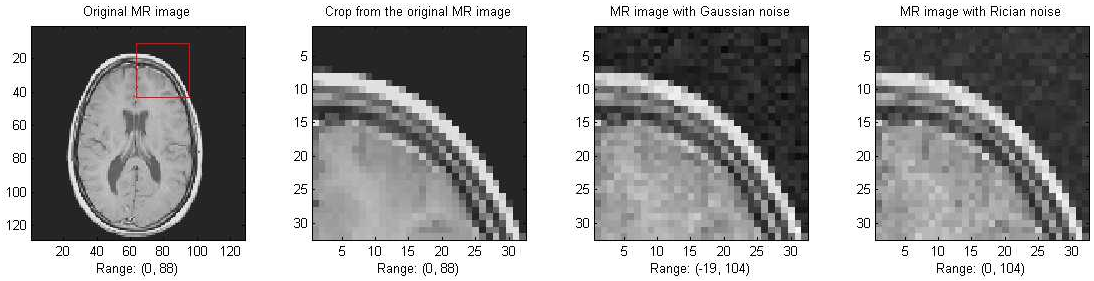

Figure 2.1: Example of MRI image with added noise (a) Original MRI image (b) Crop from the Original MRI image (c) MRI image with added Gaussian noise (d) MRI image with Rician noise distribution

As explained, it is a fact that Rician noise degrades the MRI images in both qualitative and quantitative senses, making image processing, interpretation and segmentation more difficult. Consequently, it is important to develop an algorithm to filter this type of noise. Section 4.1 gives a comparison of two of the most used methods for MRI noise removal, and their performances are assessed.

2.1.2 Partial volume effect

The partial volume effect (PVE) is the consequence of the limited resolution of the scanning hardware and the discretization procedures. It occurs in non-homogeneous areas, where several anatomical entities contribute to the graylevel intensity of a single pixel/voxel. It results in blurred intensities across edges, making difficult the task of accurately deciding on the borders of two connected objects. Figure 2.2 provides two visual examples of the explained effect: one on a synthetic image, and a real MRI slice of a hand. Another similar artifact is called *fat/water cancelling* and emerges in regions containing mutually fat and water. Due to their opposing magnetisation fields, the corresponding regions will appear dark.

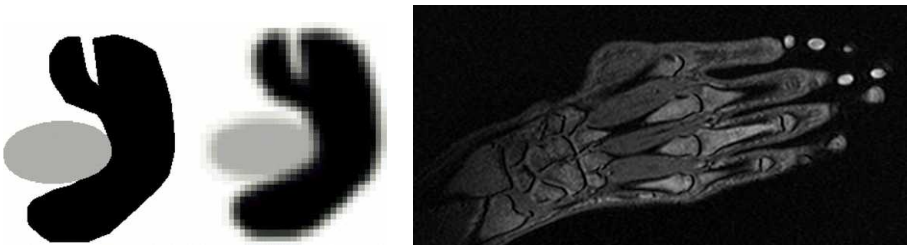

(a) (b)

Figure 2.2: Examples for the partial volume effect: (a) Synthetic image - the second image is corrupted by the PVE, resulting in difficulties for the accurate boundary extraction between regions. [51], (b)A real MR image of a hand, affected by PVE - in some regions of the image it cannot be decided the boundary between the bone and the surrounding tissue

2.1.3 Intensity inhomogeneities

Another difficulty which has to be handled by segmentation techniques using MR images is the intensity inhomogeneities shortcoming. The intensity inhomogeneities can be caused by the imperfections in the RF coil that produces the magnetic field, or by various harms in the signal acquisition procedures. Also, the magnetic field can have a nonuniform distribution due to the local magnetic properties of the studied biological structure or because of a movement of the patient during the acquisition process. This effect can be identified as a shading artefact in the image data and can have a major consequence on the performances of the intensity based segmentation algorithms, considering that a certain tissue has a constant intensity distribution in the dataset. Figure 2.3 demonstrates visually the described phenomenon. The segmentation algorithm has also to take into account other artifacts which might occur: missing parts of the bones, distorsions and essentially the variability of the graylevel distributions for the same bone, but in different postures. This effect is shown in Figure 2.4 where three different graylevel distributions are highlighted for the same bone.

Figure 2.3: Intensity inhomogeneities in MRI datasets:(a) Shaded region due to variability of the magnetic field (red arrow)m (b) Intensity distribution with respect to the variability of the bone tissue

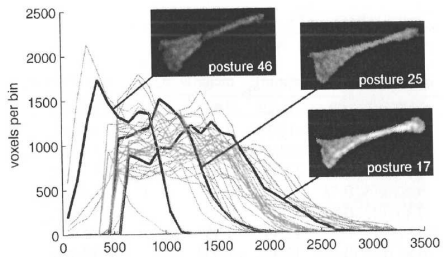

Figure 2.4: Histograms of the graylevel intensities of the same bone in different postures (Reference?)

The state of the art suggests two main methods for modelling this effect: one presumes that the tissues have distinct intensities, which vary spatially and the other tries to model this artefact as a multiplicative/additive gain field and remove it accordingly. Also, lately, new segmentation approaches which are specially designed to handle this effect have been suggested.

2.2 The human hand

The most important aspects when analysing the human hand is to study its properties and its intrinsic structure. The types and shapes of the bones which form the configuration of the hand are of interest. Also the types of the joints which interconnect the neighbouring bones are significant for the hand modelling task. Figure 2.5 provides the bone structure of the hand.

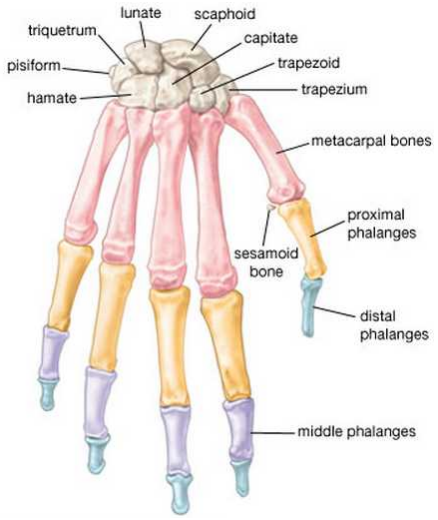

Figure 2.5: Configuration of the human hand [1].

The human hand consists of a total of 27 bones, from which eight account for the carpus (wrist), five are the metacarpal bones (creating the palm region) and the other fourteen are called phalanges and define the structure of the fingers. The metacarpal bones have a cylindrical shape and they articulate with the carpal bones on one side, and with the proximal phalanges on the other side. The phalanges can be classified in 3 categories: five proximal phalanges at the base of the fingers (the largest bones of the hand), four intermediate phalanges (one for each finger, except the thumb) and the last, five distal phalanges (at the tip of the hand). Each finger has a name for discerning reasons. Starting with the one closest to the thumb, they are named: index, middle, ring and little (pinky) finger. In this thesis only the metacarpal bones and phalanges are of interest, because they are the important parts of the hand structure providing the motion functions. For the kinematics modelling analysis, the special configuration of the joints is of higher importance, as they are essential for the wide range of hand configurations.

2.3 MRI datasets acquisition

Around 50 different postures of the hand on three subjects were scanned using a Philips Achieva 1.5T. A Philips SENSE 8-channel head coil was used for a higher signal-to-noise ratio and a more homogeneous signal in the MR image volumes. Figure 2.6 shows how the hand is placed for the MR imaging sequence and figure 2.7 display some of the hand postures of interest.

Figure 2.6: Configuration for the hand MRI sequence [60]

As the SNR is relative to the acquisition time and the volume of the voxel, for each acquisition process a balance has to be found between the scan duration and the desired resolution

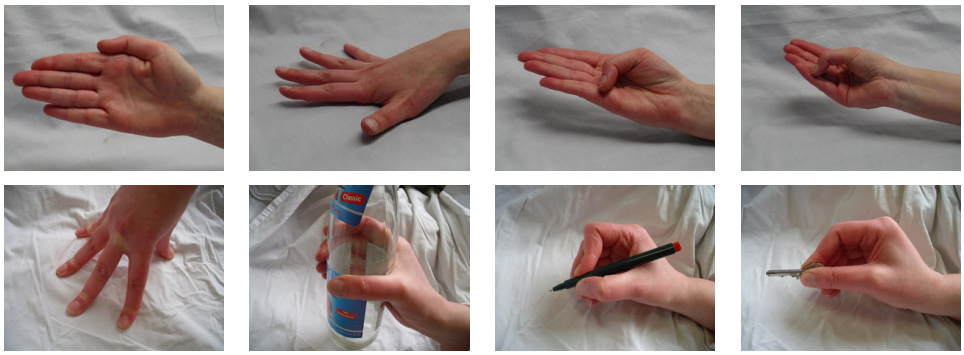

Figure 2.7: Examples of postures of the hand

(the image quality is important for the segmentation of the anatomical structures of interest and short scanning time would reduce the presence of motion artifacts and the discomfort of the subject). The conciliation was set for a scanning duration of 2 up to 2 and a half minutes per posture. Therefore, MRI volumes of size between $480 \times 480 \times 280$ and $560 \times 560 \times 212$ were aquired with a 16-bit graylevel intensity. After the acqusition, the image volumes have been interpolated, increasing the spatial resolution.

Two different sequences were used: *balancedFFE* for one subject and *turboFFE* for the other two. The *balancedFFE*, also called *trueFISP* or *balancedSSFP*, has a repetition time of 4.8ms, a time echo of $2.4ms$ a flip angle of $45°$ and a spatial resolution of $0.76mm^3$. The *turboFFE* sequence has the same characteristics but the spatial resolution is $1mm^3$.

One of the benefits of the *balancedFFE* is that it gains a high SNR at short repetition time but it can also be affected by the banding artifacts, identified as dark stripes across bones. On the other hand, the *turboFFE* has an enhanced initial appearance, but segmentation algorithms have more difficulties due to the lower spatial resolution and the different image contrast between biological structures.

Chapter 3

Segmentation techniques applied in medical imaging

Advanced medical imaging techniques require high performance segmentation algorithms. The main challenge in medical image segmentation tasks is to extract accurately the structures of interest. In the case of medical imaging the segmentation process can take place in 2D or in the 3D image domain. Usually 2D methods are applied on a single-image dataset and 3D methods are used for volume segmentation. Nevertheless, 2D algorithms can be extended to 3D medical volumes by being applied successively on the compounding 2D slices [8] [23] [38] [53]. The last approach is in some cases more practical as it is easier to implement, it requires less memory, and has lower computation complexity. This section gives an overview of the 2D and 3D most common segmentation algorithms applied in medical imaging. An overview for the implementation of each method is given and the advantages and disadvantages are discussed. It has to be mentioned that often, depending on the task, several algorithms are combined together with a view to solve difficult segmentation tasks.

3.1 Intensity thresholding algorithms

Thresholding is one of the easiest segmentation techniques for scalar images and volumes [55]. Mainly, it takes into account only the intensity value of the pixels or voxels and creates a binary partition of the dataset. *Single-threshold* algorithms use only one intensity value, called *threshold*, which separates the dataset into two classes as follows: intensities higher than the threshold are clustered in one class and the rest of the pixels (or voxels) are clustered in the other class. The mathematical formulation of the single-thresholding technique is shown in eq.

3.1, where I is the analysed intensity value and λ is the threshold. This method is also called binarization.

$$I = \begin{cases} 0 & \text{if } I \leq \lambda \\ 1 & \text{if } I > \lambda \end{cases} \tag{3.1}$$

When the analysed dataset contains more than 2 classes, a *multi-thresholding* algorithm has to be applied. In case the dataset (image or volume) has to be clustered in n different classes, $n-1$ thresholds have to be applied. The corresponding formula is displayed in eq. 3.2 where $\lambda_1 \dots \lambda_{n-1}$ are the used threshold values for differentiating the dataset in n classes represented by $val_1 \dots val_n$.

$$I = \begin{cases} val_1 & \text{if } I \leq \lambda_1 \\ val_2 & \text{if } \lambda_1 < I \leq \lambda_2 \\ \vdots & \vdots \\ val_{n-1} & \text{if } \lambda_{n-2} < I \leq \lambda_{n-1} \\ val_n & \text{if } I > \lambda_{n-1} \end{cases} \tag{3.2}$$

The difficult task is to determine the threshold values which best differentiate the regions of interest. A simple case is the one in which the structures to be clustered have contrasting intensity values (or other features). Practically, the resulting segmentation is very sensitive to the used thresholds, noise and intensity inhomogeneities (present in MRI images). Another important drawback of the approach is that it does not take into consideration the spatial distribution of the intensities. However, this method can be implemented in real-time and it is often used as an initialization step and combined with other segmentation techniques.

Adaptive thresholding is an approach which aims to improve the performance of the algorithm in images corrupted by noise and intensity inhomogeneities (MRI images). Also called *local* or *dynamic* thresholding methods [59], they compute a distinct threshold for each pixel or voxel based on the local image properties. Kittler et al. [33] used the image statistics based on the gradient magnitude for the selection of an automatic threshold, while Kom et. al [34] applied adaptive threshold in order to segment dense masses in mammograms. Other medical image segmentation applications include extracting edges and maintain only the ones which respect some predefined similarity criteria [12], segmenting blood vessels [56], extracting anatomical structures in MR images [32] and endoscopic images [64] or 3D bone segmentation in CT scans [74].

3.2 Region growing and Split and Merge algorithms

Region growing is a method which uses a predefined "growing" criteria (connectivity, intensity distribution, edges in the image) [27] in order to extract a region of interest from a scalar image or volume. Compared to the thresholding techniques, it includes information related to the neighbourhood configuration and it is designed to extract homogeneous regions which have higher probability to correspond to anatomical structures. It requires at least one *seed point* for each object to be segmented, from which selects all the belonging pixels or voxels based on the homogeneity criteria. Therefore, the main disadvantage is that it requires and is very sensitive to initialization. Results of region growing algorithms are highly influenced by noise and partial volume effects (specific for MRI images).

As in the case of the thresholding techniques, region growing is usually used in combination with other more complex algorithms. For example Zhang et. al [74] used region growing as a post-processing step for the 3D adaptive thresholding of the CT images. Also, CT angiographyic image segmentation has been realised using gradient based region growing [54]. Region growing has been improved by including topological information for 3D MRI cortex segmentation [43] or by adapting the algorithm to the fuzzy sets theory [65].

Split and merge algorithms are similar to region growing, but overcome the need of seed points [44]. Similarly, based on a predefined criteria it successively splits the regions in a certain number of subregions, and merges only the ones which satisfy the required conditions. The main drawback of this algorithm is that it requires a pyramidal grid structure of the dataset, which makes it very computationally expensive and undesirable for the huge array of data nowadays.

3.3 Classification techniques

Classifiers are usually used in pattern recognition tasks and their aim is to label the dataset based on a feature space [9]. The used features for classification of the dataset is very varied, some of the most common including image intensities or gradients. The main task when working with classifiers is to find the feature space, which best describes the dataset and can easily distinguish between the classes to be detected.

Classification techniques are known as *supervised* methods as they have to be first trained with presegmented data and then tested on new datasets for the automatic segmentation task [76]. Some of the most used classifiers in the literature are: k-nearest neighbour(kNN) (each pixel or voxel is labelled as the same class in the training dataset which is the closest in the feature space) or Parzen window (the labelling is realised based on a majority vote within a region centered at the analysed pixel or voxel). These are non-parametric classifiers since in their

implementation no assumption is made with respect to the statistical structure of the dataset. Maximum likelihood or Bayes classifier are common parametric classifiers. It is assumed that the studied feature space is formed of independent samples which form a mixture of probability distributions. Usually the distributions are Gaussian and the mixture is called finite mixture model. When it is trained, the Bayes classifier estimates the K means, covariances and the mixing coefficients, in the case of Gaussian mixtures. In the segmentation process, each pixel or voxel receives the label with the highest posterior probability.

As mentioned, it is very important for the classifiers to work with distinct quantifiable features. Practically, it is very difficult to find feature spaces which easily distinguish between the classes to be labelled. Another drawback of these techniques is that they do not perform spatial modelling, their results being vulnerable to noise corruption [68]. Also, manual interaction and gathering of the training data are very time consuming and laborious. However, as they are non-iterative, they are reasonably computationally effective and several feature spaces can be combined in the classification process.

Maximum likelihood segmentation has been applied on ultrasound images [57] where the density probability distribution and the smoothness constraints of the graylevel values are used to define the energy functional. Vrooman et. al [66] implemented the conventional kNN in combination with manual or atlas-based training for the brain tissue classification in multispectral MRI images.

3.4 Clustering techniques

Clustering algorithms are known as *unsupervised* methods and perform the same task as classifiers. The main difference is that they do not need training and they train themselves using the offered dataset by iterating between segmenting the data and defining the properties of each class. Common clustering algorithms are: K-means, fuzzy clustering and expectation-maximization (EM) [17] [9] [40] [36]. The K-means algorithm computes the mean of the feature space for each class and then allocates every pixel or voxel to the class with the closest feature vector. The algorithm minimizes the dissimilarity of each class by iteratively reassigning the pixels or voxels to the iteratively computed classes. Fuzzy c-means is a generalized version of the K-means algorithm, which allows soft segmentation based on fuzzy set theory [73] [9]. The expectation-maximization (EM) technique assumes that the data can be modelled as a mixture of Gaussians and applies the same clustering procedure. It iteratively estimates the means, covariances, mixing coefficients and computes the posterior probabilities.

Similar to classification techniques, no spatial distribution of the data is taken into account

in the clustering process, and thus their outcomes can be easily corrupted by noise and intensity inhomogeneities. As they require initial parameters, sensitivity to initialization has been shown in the literature. It also has been proved that EM has a higher initialization sensitivity in comparison with K-means and fuzzy c-means clustering [72]. Nevertheless, improved robustness to noise and intensity inhomogeneities has been demonstrated when these methods are combined with other techniques like Markov random fields and Bayesian approaches [52] [25]. In order to overcome the noise and inhomogeneity sensitivity, the performance of the clustering methods has been improved using spatial information in the minimization function [67] [15]. One of the most common application is the brain tissue segmentation in MR images [67].

Markov Random Field Modelling is not a segmentation technique, but a statistical scheme which is often used with other segmentation techniques for results improvement. The main aim of the MRFs is to include the spatial information in the segmentation process by modelling the relationships between neighbouring pixels or voxels [39]. For example, in medical image processing, this method sets constraints on the interconnectivity between pixels or voxels representing the same organ. In this case it is considered that most of the pixels or voxels can be classified the same as their neighbours, because of the very low probability of existing organs represented by a very low number of pixels/voxels.

The main disadvantages of this approach are the computational cost and the tuning of the parameters managing the strength of the spatial relationships between pixels/voxels [39]. Selecting too high parameters would result an extremely smoothed segmentation loosing important details of the structures to be segmented. Nevertheless, these algorithms are widely used in medical imaging processing, due to their ability to model also intensity inhomogeneities which are widely present in MR images [28].

3.5 Atlas guided approaches

Atlas guided techniques are widely used in medical image analysis when templates or atlases are accessible. An atlas is created using the anatomical information of the structure to be segmented. Once the atlas is generated, it is used as a reference for the segmentation algorithm, translating the process to a registration problem [42]. An initial step is to determine a transformation which maps a pre-segmented atlas structure to a configuration in the analysed image. This procedure is called *atlas warping* and is usually achieved using linear transformations [6]. Occasionally, the algorithm adapts to the anatomical variability of the studied structure by applying a sequence of linear and nonlinear transformations [16] [18] [19].

MR brain imaging is one of the most common applications of the Atlas guided approaches. The great advantage is that during the segmentation process, the labels are also transferred to

the studied dataset. On the other hand, these techniques have proved difficulties in segmenting very complex structures. Also the results provided by these algorithms are affected by the variability of the anatomical structures between subjects. This is the reason for which their usage is recommended for structures which are stable over the studied population. An improvement has been proposed by Thompson and Toga [63] by using probabilistic atlases, but this approach is more computationally expensive and requires manual interaction.

3.6 Mathematical morphology and Watersheds

Mathematical morphology is a technique for analysing geometrical structures in image processing tasks. Originally defined only for binary datasets, their functions have been later enlarged for the use on grayscale data. This technique measures how a predefined shape, called *structuring element*, fits or misses the structures in the studied dataset. Examples of used structuring elements in medical image analysis are discs, circles and squares (in the 2D case), and spheres and cubes (in 3D) [58]. The choice of the structuring element is very significant for the segmentation process, as the results strongly depend on the size and shape of the chosen local neighbourhood template. Summarizing the basic procedures, the two main used morphologic operations are dilation and erosion [45]. For example, having defined a 3×3 square structuring element, as shown in eq. 3.3, the related dilation and erosion operations are described in eq. 3.4, where A denotes the binary image to be analysed, ϕ is the empty set and $y + S = \{y + s | s \epsilon S\}$.

$$S = \{(i, j) \epsilon Z^2 | i, j = -1, 0, 1\} \tag{3.3}$$

$$\begin{aligned} D_s &= \{y \epsilon Z^2 | y + S \cap A \neq \phi\}, \\ E_s &= \{y \epsilon Z^2 | y + S \subseteq A\} \end{aligned} \tag{3.4}$$

The operators defined in eq. 3.4 can provide useful information on the edges and the boundaries of the existing structures in the analysed dataset, which can be further used in the segmentation process. Also, the combination of the two operators provides two additional morphological transformations: *opening* (erosion followed by dilation using the same structuring element) and closing (dilation followed by erosion) [11]. Practically, using the closing transformation, small holes or gaps are reduced; while opening removes narrow connectors (can better distinguish the studied structures) or opens large holes. Morphological operators can not be considered standalone segmentation techniques, but they are usually used as a step in the segmentation workflow.

The morphological approach for medical image segmentation merges region growing and

edge detection algorithms. Pixels/voxels which are situated close to a regional minima of the intensity function are grouped together and the borders between two neighbouring groups are defined along the high gradient values of the image. This method is called *watershed transformation* and its applicability has been extended to grayscale images as well. In the case of a 2D image, based on the intensity value, every pixel can be classified in one of the three groups:

- a) pixels placed in a local minimum
- b) pixels placed in the neighbourhood of a local minimum
- c) pixels placed equally between several local minimum points

For a particular local minimum, a *catchement basin* is formed from the set of pixels satisfying the second condition (also called the *watershed* of the local minimum). The points belonging to the third group are defining the *watershed lines*. The main goal of the watershed segmentation techniques is to determine the catchement basins, whose local minima represent structures of interest in the analysed image, and the watershed lines, providing the boundaries of the structures. The great disadvantage of this approach is that usually it over-segments the images, particularly in the case of noisy images (MRI datasets). This leads to additional pre-processing or post-processing stages (for example to merge the resulted regions based on a similarity criteria) which might require manual interaction, which is time consuming. Therefore, in order to reduce over-segmentation, Najman and Schmitt [46] suggested the use of morphological operators.

Dogdas et al. [2] proposed a sequence of morphological operations for the 3D skull segmentation in MR images. Also, morphological operators have been widely used as a pre-processing step for splitting connected distinct structures (it is also the case of two bones connected due to the noise in the image dataset) [3]. Watershed techniques using prior information [26] and probabilistic atlases [61] have been also successfully used in medical image segmentation tasks.

3.7 Active contours

Active contour methods can intuitively be understood as digitally-generated curves operating within images with the aim of identifying object boundaries. Initially named snakes [31] , they are energy minimizing splines, moulding a closed contour to image object boundaries by means of deformation under the influence of image forces, internal forces and external constraint forces.

Considering that the snake (contour) position at time t can be parametrically represented by $v(s,t) = (x(s,t), y(s,t))$, the evolution of the deformable model can be represented as shown in eq. 3.5, where $\mu(s)$ and $\gamma(s)$ control the mass and the damping density of the contour. The

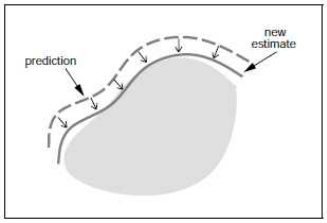

Figure 3.1: Shape prediction using active contours

model is moving under the influence (magnitude and direction) of the internal and external forces.

$$\mu(s)\frac{\delta^2 v(s,t)}{\delta t^2} + \gamma(s)\frac{\delta v(s,t)}{\delta t} = F_{int} + F_{ext} \tag{3.5}$$

The most commonly used formulation for the internal energies is shown in eq. 3.6, where $\alpha(s)$ and $\beta(s)$ manage the tension and the flexibility of the contour [31]. The external potentials are defined based on the gradients or other features in the image.

$$F_{int} = \frac{1}{2}(\alpha(s)|\frac{\delta v(s,t)}{\delta s}|^2 + \beta(s)|\frac{\delta^2 v(s,t)}{\delta s^2}|^2) \tag{3.6}$$

Some of the disadvantages of this approach are the sensitivity of the snake evolution to the initialization and poor convergence in concave regions. Improvements have been made by Xu and Prince [71]. Using the gradient vector flow (GVF) their method has better performance in near concave boundaries and lower sensitivity to initialization. Another drawback of the snakes approach is that it can not handle the correct segmentation of multiple objects in one iteration and it also proves to have self-intersection difficulties (it can not control topology changes). This is due to the explicit (parametric) representation of the contour to evolve towards the boundaries of the objects to be segmented.

An alternative method for defining active contours was introduced by Osher and Sethian [49]. *Level Set* methods employ the implicit representation of the contours, the curves being defined by the *zero crossings* of a *characteristic* function, called *Level Set* function. The pure mathematical description of the function is shown in eq. 3.7, where C is the extracted contour, (x, y) are the coordinates of the points (the 2D case is considered) and $\phi(x, y)$ is the Level Set function.

$$C = \{(x, y)|\phi(x, y) = 0\} \tag{3.7}$$

The Level Set function $\phi(x, y)$ evolves, similar to the snakes methods, based on artificial

forces, which make the front move in the normal direction. The progressing contour can be extracted at any moment from the zero level set, as shown in eq. 3.7. Some of the advantages of the Level Sets in comparison with the snakes approach can be concluded: implicit representation (no parametrization), allows changes in topology of the evolving contour and can easily represent various geometrical shapes in different number of dimensions (2D and 3D).

Active contours methods have been widely applied in medical image segmentation tasks [22] [21] [35]. Their ability to adapt contours to structures with irregular shapes made them applicable for brain segmentation tasks [7] or tumour region detection. They were also used for segmenting 3D volumetric MRI datasets for image guided surgery tasks [10]. Chunming Li et al. [37] proposed an improvement of the variational level set methods in the case of medical datasets corrupted by intensity inhomogeneities which has significant results on bone segmentation in X-ray images. Jiang [30] combined in his work the active contours approach with morphological operations for the X-ray bone fracture subtraction. Local structure [69] and texture [41] descriptors have been also incorporated in the evolution of the active contours for bone segmentation in CT datasets.

Chapter 4

Methodology

4.1 Image pre-processing

4.1.1 Denoising MRI images using wavelets

One of the important applications of wavelets is image denoising and compression. By computing the Discrete Wavelet Transform (DWT) the image content is decomposed in *scaling* coefficients (approximation subband) and *wavelet* coefficients (detail subband) at different orientations (horizontal, vertical and diagonal) and resolutions. One of the characteristics of the DWT is that it tends to concentrate the information contained in the analysed signal into a relative small number of coefficients. In the case of a noisy image, the DWT will contain a reduced number of coefficients with high SNR and many coefficients with low SNR. The main noise reduction algorithm based on DWT decomposition is to discard low SNR coefficients and to keep the significant ones. After selecting the desired coefficients, the Inverse Discrete Wavelet Transform (IDWT) provides the noise suppressed image. Nevertheless, the DWT is not time space invariant, simple miss-alignments between the signal and the wavelet basis function providing artifacts in the denoised image. This drawback is solved by using the Shift-invariant Wavelet Transform (SWT). Several properties which make the wavelet transform suitable for the denoising task, are summarised below:

- *multiresolution* - the multi-level wavelet decomposition allows the analysis of image details at different scales;
- *edge detection* - high wavelet coefficients correspond to image edges;
- *edge evolution across scales* - the wavelet coefficients corresponding to image edges tend to persist across the scales.

The main task is to find a suitable threshold in order to select the coefficients which best describe the information in the analysed image and to suppress as much noise as possible. In the case the threshold is too low, the noise suppression might be unsatisfactory, but loss of image detail (excessive smoothing) would be visible in the case of a high threshold.

Many techniques have been proposed in the literature with a view to find the best suitable threshold for the wavelets coefficients and for noise level estimation in MRI images. A survey of the methods used for noise estimation is given by Aja-Fernandes et al [5]. There are summarized methods which are using background regions in the MRI image for the noise distribution estimation [29] [4] as well as techniques which model the Rician noise distribution using the square of the magnitude MRI image [47].

One of the most used method for denoising MRI images by thresholding the wavelet coefficients is the one proposed by Donoho [20]. He showed that a *global threshold*, defined in eq. 4.1, is asymptotically optimal, where N is the size and σ is the noise standard deviation of the wavelet coefficient arrays.

$$\lambda = \sigma\sqrt{2\log N} \tag{4.1}$$

Taking into account that the *universal threshold* is computed globally using the coefficients at all scales, the resulting denoised images are usually over-smoothed. To overcome this problem, the *balance-sparsity norm* approach can be used for defining an optimal threshold. A thresholds array t is defined as having uniformly distributed values between 0 and 1. Using the t array, two curves are defined: the percentage of *2-norm recovery* (the measure of the energy loss after the denoising process using the values in t) and the percentage of the *relative sparsity* (the number of resulting 0 coefficients in the denoised image). The two curves intersect at the t_{opt} and the *square root balance-sparsity norm* threshold is defined using eq. 4.2, where c is the number of detail coefficients.

$$\lambda = \frac{\sqrt{t_{opt}/c}}{c} \tag{4.2}$$

After an optimal threshold is computed, it can be applied to the wavelet coefficients in two different manners:

- *Hard* thresholding is the simplest method and it sets to zero all the coefficients which are smaller than the threshold and keeps the others. Considering c the array of wavelet coefficients to be thresholded, the mathematical definition is shown in eq. 4.3:

$$\overline{c}_h(k) = \begin{cases} sign(c(k))(|c(k)|) & \text{if } |c(k)| > \lambda \\ 0 & \text{if } |c(k)| \leq \lambda \end{cases} \tag{4.3}$$

- *Soft* thresholding is an extension of the hard thresholding method, first discarding the coefficients which are smaller than the threshold, and scaling the remaining ones. This method has better mathematical properties because it does not create discontinuities at $c(k) = \pm\lambda$ comparing the the hard procedure which does. The equation defining the soft shrinkage rule is given in eq. 4.4:

$$\overline{c}_s(k) = \begin{cases} sign(c(k))(|c(k)| - \lambda) & \text{if } |c(k)| > \lambda \\ 0 & \text{if } |c(k)| \leq \lambda \end{cases} \tag{4.4}$$

The effects of the thresholding methods defined in eq. 4.3 and 4.4 applied on a linear signal can be visualized in Fig. 4.1 (the used threshold is $\lambda = 1$ for a linear signal defined in the range $[0, 2]$).

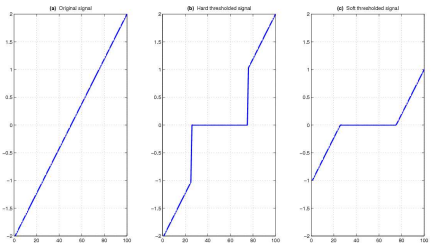

Figure 4.1: Thresholding of a linear signal using (b) Hard Thresholding or (c) Soft Thresholding

The proposed method for MRI image denoising using wavelets is sumarised in Algorithm 1 and consists in the following steps:

Algorithm 1: MRI image denoising using wavelets

1. Choose a type of wavelet ('Haar','Daubechies','Symlets','Biorthogonal wavelets') and the number of levels of decomposition (scales) and compute the DWT (or SWT) of the image to be denoised.
2. Compute an optimal threshold using eq. 4.1 or 4.2.
3. Select one of the shrinkage methods (eq. 4.3 and 4.4) and apply the threshold to the wavelet coefficients accordingly.
4. Compute the IDWT (or ISWT) using the thresholded coefficients and determine the denoised image.

4.1.2 Nonlinear anisotropic filtering

One common technique used in image processing to decrease the noise is the scale-space procedure firstly introduced by Witkin [70]. It refers to creating a family of images using the convolution of the original image with an isotropic Gaussian filter of different widths. The process is called *linear diffusion* and results in a family of increasingly blurred images, as the standard deviation of the Gaussian kernel increases. This method has a main drawback as it reduces the noise, it also degrades the details in the original image.

Perona and Malik [50] proposed a technique, called *anisotropic diffusion*, which reduces the image noise but preserves or even enhances the features in the image (e.g. edges, lines) which are of high interest in image processing tasks. The suggested filter can be expressed as a diffusion process which gives preference to intraregion instead of interregion smoothing. The novelty is that the diffusive procedure is controlled by a variable diffusion coefficient, which limits the smoothing in areas of interest (edges, boundaries). The general mathematical formulation of the mentioned technique is given in eq. 4.5, where $c(x, y, t)$ is the diffusion coefficient, $I(x, y, t)$ is the image intensity and *div* and ∇ are the divergence and the gradient operators. The spatial coordinates of the image are represented by x and y (in the 2D case), and t corresponds to the time parameter, which in discrete implementation is the iteration number.

$$\frac{\partial}{\partial t} I(x, y, t) = div(c(x, y, t) \nabla I(x, y, t)) \tag{4.5}$$

The main difficulty is to choose the proper diffusion coefficient. It is defined as a positive monotonically decreasing function of the image gradient which, ideally, has to be 0 at edges and 1 when the filter is located at the interior of a region. Practically, $c(x, y, t)$ has to encourage the forward diffusion inside smooth regions (small variations like noise and useless texture have to be removed), and backward diffusion at high gradient locations (preserving and even sharpening the boundaries and the features of interest). Perona and Malik [50] proposed two mathematical functions for the diffusion coefficient, where the first one (eq. 4.6) advantages the high contrast edges rather than the low contrast ones, and the second one (eq. 4.7) favours the wide areas instead of narrow ones.

$$c_1(x, y, t) = exp\left(-\left(\frac{|\nabla I(x, y, t)|}{\kappa}\right)^2\right) \tag{4.6}$$

$$c_2(x, y, t) = \frac{1}{1 + \left(\frac{|\nabla I(x, y, t)|}{\kappa}\right)^2} \tag{4.7}$$

In eq. 4.6 and 4.7 κ is called the *conductance parameter* and has to be chosen accordingly

so the anisotropic diffusion process can distinguish between an edge and an intensity value corrupted by noise. Usually it is selected empirically, or, when it is the case, it is defined using a noise estimator.

The numerical scheme which implements the eq. 4.5 defines the intensity change at location (x, y) after one iteration as a sum of contributions of the neighbouring pixels weighted by the corresponding directed flow components (defined in eq. 4.8), as shown in eq. 4.9.

$$\begin{aligned}
\Phi_E(x,y,t) &= c(x+\frac{dx}{2},y)[I(x+dx,y)-I(x,y)] \\
\Phi_W(x,y,t) &= c(x-\frac{dx}{2},y)[I(x,y)-I(x-dx,y)] \\
\Phi_N(x,y,t) &= c(x,y+\frac{dy}{2})[I(x,y+dy)-I(x,y)] \\
\Phi_S(x,y,t) &= c(x,y-\frac{dy}{2})[I(x,y)-I(x,y-dy)]
\end{aligned} \tag{4.8}$$

$$I(x,y,t+dt) = f(x,y,t) + dt\left[\frac{1}{dx^2}[\Phi_E(x,y,t)-\Phi_W(x,y,t)] + \frac{1}{dy^2}[\Phi_N(x,y,t)-\Phi_S(x,y,t)]\right] \tag{4.9}$$

It has to be mentioned that in eq. 4.8 and 4.9 dx and dy represent the pixel spacing in the intensity image accounting for the anisotropy of the procedure. This suggests that, at a certain location, closer pixels contribute more than the ones located at a higher distance. Also, the aforementioned numerical scheme refers to a 4-pixel connectivity. For a better isotropy, it can be easily extended to 8-pixel connectivity, by adding the contribution of the diagonal neighbouring pixels (placed at a distance $\sqrt{dx^2+dy^2}$) or even to 26-pixel connectivity in the case of 3D image datasets. In eq. 4.9 the integration constant dt is introduced. For numerical stability reasons it has to be chosen with respect to a stability criteria. It depends on the number of neighbouring pixels/voxels and a full list of integration constants, considering the connectivity structure, is provided in [24] .

Several experiments have been conducted to test the two denoising methods on a synthetic image corrupted by Rician noise and a real MR image of the hand. Figure 4.6 gives a comparison of the performances of a *geodesic active contour* algorithm applied on a synthetic image corrupted by Rician noise, the wavelet denoised image and the anisotropic diffused one. The goal is to detect as accurate and fast as possible the boundaries of the inner circle with the same parametrized active contour algorithm.

In Figure 4.6 , the first row (4.2(a),4.2(b),4.2(c)) displays the initial contour, which is the same for all the images. The second row (4.2(d),4.2(e),4.2(f)) shows the intermediary stages

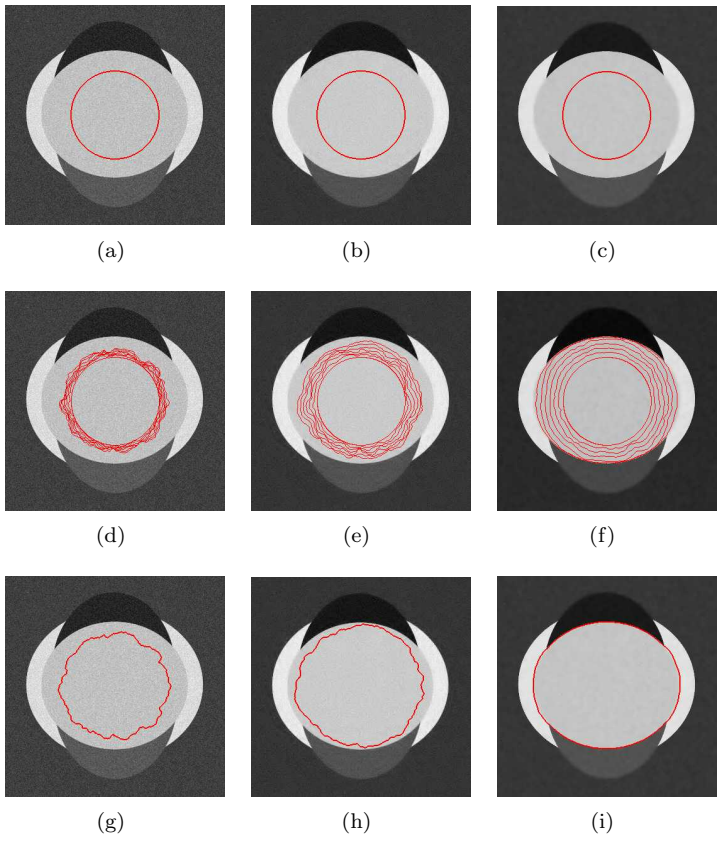

Figure 4.2: Performance of an active geodesic contour algorithm on an image corrupted by Rician noise and the denoised versions using wavelets and anisotropic diffusion

of the contour for each image and the last one (4.2(g),4.2(h),4.2(i)) plots the final achieved shape. It has to be mentioned that in all the three cases the algorithm has run for the same number of iterations (350). The denoised image using the wavelet approach was obtained using a *Daubechies* mother wavelet and *soft-thresolding* using the *balance-sparsity norm* threshold defined in eq. 4.2. The anisotropic diffusion filtering was realised with $\kappa = 30$ and 5 iterations.

From the analysis of the results displayed in Figure 4.6 it can be concluded that the geodesic active contour algorithm performs the best on the anisotropic diffused image. It also converges faster to the shape of interest and this is because of the properties of the anisotropic diffusion, to smooth the big regions, with similar intensity distributions, and to maintain the intra-region features (edges). When the active contour algorithm performs on a smoothed area, it evolves faster towards its boundaries, as the speed variable depends on the gradient values of the region of interest. Further on, Figure 4.3 provides an analysis of the same problem on a real MRI image,

assessing the performance of the bone segmentation approach using active contours.

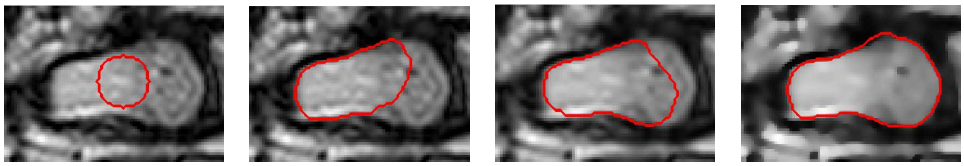

(a) (b) (c) (d)

Figure 4.3: Performance of the bone segmentation approach using an active geodesic contour algorithm on a real MR image: (a) Initialization with a circle of radius 10; Result of the segmentation process obtained on (b) the original image, (c) the wavelet denoised image and (d) the anisotropic diffused image.

In Figure 4.3 the denoised images were generated using a *Daubechies* mother wavelet and *soft-thresolding* using the *balance-sparsity norm* threshold in the case of the wavelet denoising approach and a parametrization of $\kappa = 25$ and 5 iterations for the anisotropic diffusion process. It can be concluded that while the segmentation algorithm extracts only a part of the bone in the case of the wavelet denoised image (Figure 4.3(c)), the whole bone region is extracted in the case of the nonlinear filtered image (Figure 4.3(d)). The segmentation algorithm has run with the same parameters and the same number of iterations (1000) in all the cases presented in Figure 4.3.

Taking into account the results discussed in Figure 4.6 and Figure 4.3 the nonlinear filtering approach will be used for the final implementation as a preprocessing step (noise reduction and edge enhancement). It has been proved that the anisotropic diffusion has several advantages in comparison to the wavelet denoising procedure. The diffusive technique produces more smoothed big regions (with similar intensity distributions) which help the active contour algorithm to converge faster. Also it does not have any constraints on the size of the image to be analysed; the wavelet denoising procedure requests that the image sizes have to be multiple of 2^L, where L is the number of decomposition levels (in all the conducted tests, 4 scales were used). This requirement limits the use of this procedure for cropped images or for analysing images which do not respect the demanded condition. Finally, the anisotropic filtering method can be easily expanded to 3D image datasets (26-connectivity), as explained in Section 4.1.2.

4.2 Initialization

For a good segmentation of the bone structures in the MRI 3D datasets, an appropriate initialization is required. It does not have to be very accurate, but it has to provide starting contours (or volumes for the 3D case) for each bone to be segmented. Two elementary approaches

are considered for this stage: thresholding, using the *single-thresholding* method explained in section 3.1, or clustering using *Fuzzy C-means*.

Thresholding is a straightforward procedure. Based on visual inspection of the distribution of the graylevel intensity values in the 3D image volume, the user has to select a threshold which would distinguish the best between bone structures and the surrounding tissues. As mentioned in section 3.1, it is very difficult to determine a good threshold value and this process is very sensitive to noise and intensity inhomogeneities.

Fuzzy C-means clustering is a method which allows the splitting of a dataset into several classes. The user has to set the number of desired clusters, and every pixel/voxel in the dataset, based on its features, is assigned to the closest class. This technique has been widely used in medical image segmentation tasks, and the clustering of the pixels/voxels is derived from their graylevel intensity values. Considering that each cluster is characterized by its mean value v_m and I_n is the intensity gray value of a pixel/voxel, *Fuzzy C-means* clustering implements the minimization of the cost function in eq. 4.10, where μ_{mn} is a membership function, specific to the fuzzy theory, which defines the degree of membership of the n^{th} pixel/voxel to the m^{th} class ($n = 1..N$, where N is the number of pixels/voxels in the dataset and $m = 1..C$ is the cluster number). The degree of fuzziness of the resulting segmentation is decided by the l parameter, with $1 \leq l < \infty$.

$$J = \sum_{n=1}^{N} \sum_{m=1}^{C} \mu_{mn}^{l} ||I_n - v_m||^2 \tag{4.10}$$

The membership function μ_{mn} is defined in the $[0, 1]$ interval and the constraint $\sum_{m=1}^{C} \mu_{mn} = 1$ has to be fulfilled. The clustering algorithm carries an iterative optimization procedure of the cost function in eq. 4.10 by updating the membership function μ_{mn} and the mean values of each cluster v_m using the mathematical formulations in eq. 4.11 and 4.12.

$$\mu_{mn} = \frac{||I_n - v_m||^{-2/(l-1)}}{\sum_{k=1}^{C} ||I_n - v_k||^{-2/(l-1)}} \tag{4.11}$$

$$v_m = \frac{\sum_{n=1}^{N} \mu_{mn}^{l} I_n}{\sum_{n=1}^{N} \mu_{mn}^{l}} \tag{4.12}$$

The *Fuzzy C-means* algorithm stops when the cost function in eq. 4.10 reaches a local minimum, depicting that the inter-cluster disparity is maximised and the intra-cluster dissimilarity is minimized. As a result, the voxels close to the mean value of the assigned class have a high membership value and the ones far from the centroid have low membership value. As an example, the *Fuzzy C-means* clustering algorithm was applied on a MRI slice of the human hand, shown in Figure 4.4(a). The number of clusters is set to 3 (considering that there are

three main clusters: background, soft tissues and bone), and the resulting bone class is provided in Figure 4.4(b). For comparison, Figure 4.4(c) provides an initialization resulted from a *single-thresholding* procedure, using a threshold computed with the Otsu method.

(a) (b) (c)

Figure 4.4: Example of the initialization procedure using *Fuzzy C-means* clustering and thresholding; pixels in white are classified as bone pixels

Analysing the initialization results provided in Figure 4.4, it can be concluded that *Fuzzy C-means* clustering performs better than *single-thresholding*. In Figure 4.4(c) some of the bone structures are not detected, while in Figure 4.4(b) most of the bone pixels are identified. It is obvious that in both cases, some of the soft tissues are also classified as bone, due to their graylevel intensity value. These areas can be easily discarded based on measurements of the properties of the analysed region (in the 2D case), or by visual inspection in the 3D case (only the bone shaped volumes are kept).

4.3 Level set methods

Level set methods were firstly introduced by Osher and Sethian [49] and have been widely used in medical image segmentation applications, mainly because of their ability of tracking the boundaries of the biological structures of interest. Some of their facilities include the intrinsic representation of the contours which provides flexibility to topological changes, and their superior numerical stability, which make them suitable for the extension of their applicability to 3D datasets.

When referring to implicit representation, it means that a contour $\Gamma(t)$, which is supposed to evolve towards the boundaries of the desired object, is defined as the zero level set of an embedding-function $\phi(x, y, t) : \mathbf{R}^3 \times \rightarrow \mathbf{R}$ as given in eq. 4.13.

$$\Gamma(t) = \{(x, y) | \phi(x, y, t) = 0\} \tag{4.13}$$

Using the contour defined in eq. 4.13, other two domains can be defined: $\Omega^+ = \{(x,y)|\phi(x,y,t) > 0\}$, called the *interior* of Γ, and $\Omega^- = \{(x,y)|\phi(x,y,t) < 0\}$, named the *exterior* of Γ.

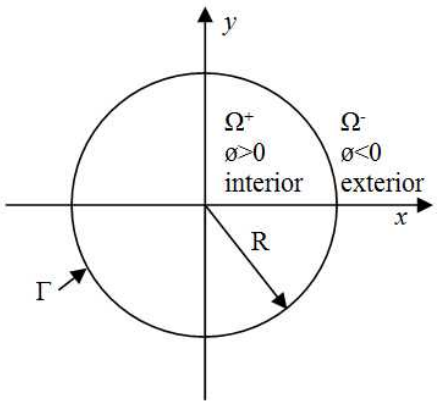

Figure 4.5: Implicit representation of a circle of radius R, defining the contour Γ, the interior domain Ω^- and the exterior domain Ω^+

In the case of Figure 4.5 the embedding-function is defined on the whole domain as $\phi = x^2 + y^2 - R^2$ and the contour Γ is defined as the zero level set of ϕ.

In practice the Level Set function $\phi(x,y,t)$ is generated using the signed Euclidian distance function. The distance $d(x,y)$ is defined as the length of the shortest path form the point (x,y) to the contour Γ. Therefore, the interface can be defined as shown in eq. 4.14:

$$\phi(x,y,t) = \begin{cases} -d(x,y,t) & : (x,y) \in \Omega^- \\ 0 & : (x,y) \in \Gamma(t) \\ d(x,y,t) & : (x,y) \in \Omega^+ \end{cases} \tag{4.14}$$

Having the Level set function defined, two other concepts can be introduced: $\overrightarrow{N}$, the outer unit normal vector, in eq. 4.15, and κ, the mean curvature, in eq. 4.16, where div is the divergence operator and $|\nabla\phi|$ is the Euclidean norm.

$$\overrightarrow{N} = -\frac{\nabla\phi}{|\nabla\phi|} \tag{4.15}$$

$$\kappa = div\frac{\nabla\phi}{|\nabla\phi|} \tag{4.16}$$

The interface Γ evolves in time due to several artificial forces, which make the contour move in the normal direction. The evolution of the curve with a normal velocity $\overrightarrow{V}$ is given by the PDE in eq. 4.17, called the *fundamental level set equation*. The velocity can be influenced

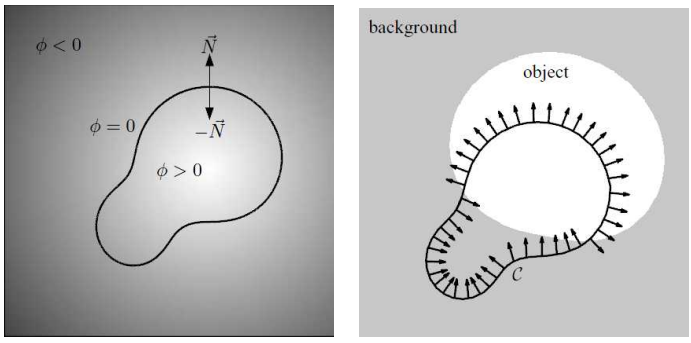

(a) (b)

Figure 4.6: (a) Level set conventions introduced in eq. 4.15 and 4.16 (b) Evolution of the contour under the influence of the artificial forces

by an external generated velocity field, an internal generated velocity field ($\overrightarrow{V} = V_n \overrightarrow{N}$) or the mean curvature ($\overrightarrow{V} = -b\kappa\overrightarrow{N}$; b is a weighting parameter of the mean curvature), and, based on the sign, it can determine the contour to progress inwards or outwards. It has to be mentioned that the interface moves always in its normal direction, as moves in tangential directions would not produce any changes in the shape of the curve. Concluding, in the level set framework, the main purpose is to solve specific Partial Differential Equations (PDEs) as the one defined in eq. 4.17.

$$\frac{\partial \phi}{\partial t} + \overrightarrow{V}|\nabla \phi| = 0; \tag{4.17}$$

Due to their applicability in medical image segmentation tasks, several types of active contour models appear in the literature. A rough classification can divide the active contours models in two classes: boundary-based and region-based. Each of these models have their own advantages and disadvantages, depending on the segmentation task, which will be further on explained.

4.3.1 Boundary-based level sets

Boundary-based level set methods are active contours which take into account the image intrinsics for the evolution of the curve towards the boundary of the object to be detected. A representative implementation using this approach is the one proposed by Caselles et. al. [13] which performs contour length minimization in a Riemannian space making use of intrinsic geometric data in the image space. One of the advantages of this method is that it is a fusion of the classical energy minimization approach introduced by snakes (discussed in section 3.7) and the theory of contour propagation using geometric information, providing high and stable

boundary localization. The curve evolution PDE proposed by Caselles et. al. [13] is formulated in eq. 4.18, where I is the image domain and c is a nonnegative real constant.

$$\begin{aligned} \frac{\partial \phi}{\partial t} &= g(I)|\nabla\phi| div\left(\frac{\nabla\phi}{|\nabla\phi|}\right) + c\nabla g(I)|\nabla\phi| \\ &= g(I)(c+\kappa)|\nabla\phi| \end{aligned} \tag{4.18}$$

The evolution of the curve is influenced by a general-edge detector function,$g(I)$, which generates an image dependent force. The objective of this term is to accurately lead the evolution of the curve toward the desired boundaries, and to stop the progress once the borders are achieved. It can be defined in different manners, depending on the features of interest in the image, with the condition that it has to be positive defined and monotonically decreasing such that,

$$\lim_{z\to\infty} g(z) = 0 \tag{4.19}$$

One common edge-indicator function, depending on the image gradient, is displayed in 4.20, where $G_\sigma * I(x,y)$ is a smoothed version of the image using a Gaussian of σ standard deviation and $p \geq 1$ (the higher p, the steeper edge-indicator function). It has to be noted that g complies with the condition in eq. 4.19. This implies that for high gradients in the image (at edges), $g = 0$ and the curve evolution stops as it converges towards the desired boundaries.

$$g(|\nabla I(x,y)|) = \frac{1}{1+|\nabla G_\sigma(x,y) * I(x,y)|^p} \tag{4.20}$$

Another term of high importance in eq. 4.18 is $(c+\kappa)|\nabla\phi|$ which makes the level set moving in the normal direction of the curve acting as an internal force. The mean curvature κ helps the smoothing and the length minimization of the interface, as it incorporates geometrical information, and the constant parameter c creates a *balloon force* which pulls the front in the direction of the desired objects and also facilitates the capture of concave shapes.

In this approach the resulting segmented object is influenced only by the gradients in the image. This can lead to defective results of the segmentation algorithm, as the contour can stop at a local minimum (as high gradients can be placed anywhere in the image, especially in the case of noisy images) or can "leak" out of the structure of interest in a region where the boundaries are not well defined. For these reasons, this segmentation technique is consistent when it is applied on datasets where the edges of the structures to be segmented represent the salient features.

4.3.2 Region-based level sets

Region-based level set methods try to deal with the leakage problem based on the Mumford-Shah functional which attempts to split the image in two distinct regions (foreground and background) based on a statistical approach. One of the most representative techniques which implements level set evolution using region information is the Chan Vese model [14]. The functional describing this model is shown in eq. 4.21.

$$\varepsilon(\phi, \mu_{int}, \mu_{ext}) = \lambda_1 \int_\Omega (I-\mu_{int})^2 H(\phi) d\Omega + \lambda_2 \int_\Omega (I-\mu_{out})^2 (1-H(\phi)) d\Omega + \alpha \int_\Omega H(\phi) d\Omega + \beta \int_\Omega |\nabla H(\phi)| d\Omega \tag{4.21}$$

The first two terms in in eq. 4.21 refer to the distribution of the intensity levels in the exterior and the interior of the level set, which are represented by the mean values of the two regions (eq. 4.22), the third one refers to the area outside the level set and the last term represents the length of the curve. $H(\phi)$ is the Heaviside function described in eq. 4.23, being 0 in the inner region and 1 otherwise. The image domain is represented by Ω and $\alpha \geq 0, \beta \geq 0, \lambda_1 > 0, \lambda_2 > 0$ are fixed parameters.

$$\begin{aligned} \mu_{int} &= \frac{\int_\Omega I H(\phi) d\Omega}{\int_\Omega H(\phi) d\Omega} \\ \mu_{ext} &= \frac{\int_\Omega I(1-H(\phi)) d\Omega}{\int_\Omega (1-H(\phi)) d\Omega} \end{aligned} \tag{4.22}$$

$$H(\phi) = \begin{cases} 0, & \text{if } \phi < 0 \\ 1, & \text{if } \phi \geq 0 \end{cases} \tag{4.23}$$

Using the previously defined functional (eq. 4.21) the associated partial differential equation describing the evolution of the level set is derived in eq. 4.24, with the Dirac function $\delta(\phi) = \frac{\partial H(\phi)}{\partial \phi}$.

$$\frac{\partial \phi}{\partial t} = \delta(\phi) \left[\lambda_2 (I-\mu_{ext})^2 - \lambda_1 (I-\mu_{int})^2 - \alpha + \beta div \left(\frac{\nabla \phi}{|\nabla \phi|} \right) \right] \tag{4.24}$$

The mean intensity values for the inner and outer regions, μ_{int} and μ_{ext}, of the level set are not previously defined. They are computed from the initialization of the curve and updated after each iteration. For each point, the distance to the two mean values is computed, and the curve is moved in such a way that the point is assigned to the region with the closest average intensity value. The algorithm is considered to converge when, after the mean values

are updated, no points are reassigned. When the solution acquires the steady state, the contour which best separates the two regions (background and foreground) is determined by the zero level set of the embedding function ϕ.

This approach has many advantages over the edge-based approach. It is robust when segmenting regions with high noise, it can identify regions with fuzzy boundaries (very smooth) and does not need any prior knowledge of the region to be segmented (mean intensity value). On the other hand, it is limited to the segmentation of two regions (foreground and background) and the global character of the mean values μ_{int} and μ_{ext} may lead to erroneous segmentation of objects with complex distributions of the intensity values.

4.3.3 Hybrid level set method

For an accurate segmentation of the bone structures in the MRI datasets, a hybrid level set approach is employed. The main scope is to combine the capabilities offered by the region-based and the edge-based level set methods in the interest of obtaining good segmentation results on real MR images. This procedure was introduced by Zhang et. al [75] and the proposed partial differential equation which describes the evolution of the contour is given in eq. 4.25, where μ denotes the lowest graylevel intensity value which distinguishes the object to be segmented from the background, and $g = g(|\nabla I|)$ is the edge-indicator function introduced in 4.20.

$$\frac{\partial \phi}{\partial t} = \delta(\phi) \left[\alpha(I - \mu) + \beta div \left(g \frac{\nabla \phi}{|\nabla \phi|} \right) \right] \tag{4.25}$$

In the PDE given by eq. 4.25 the first term includes the region-based level sets approach, advancing the contour towards areas with graylevel intensity values higher than μ, and the second expression comprises the edge-based method which makes the interface evolve in the direction of high image gradients. The contribution of each term of the PDE to the evolution of the level set embedding function is weighted using the parameters α and β. Using the PDE proposed by Zhang et al. in eq. 4.25 and the Chan Vese model proposed in eq. 4.24 the functional for the aforementioned hybrid model can be defined in eq. 4.26.

$$\frac{\partial \phi}{\partial t} = \delta(\phi) \left[\lambda_2 (I - \mu_{ext})^2 - \lambda_1 (I - \mu_{int})^2 + \beta div \left(g \frac{\nabla \phi}{|\nabla \phi|} \right) \right] \tag{4.26}$$

This curve evolution described in eq. 4.26 allows the level set algorithm to evolve inside the object of interest, but restricts the progress at high image gradients and also smooths the curve at weak edges. Another situation which has to be taken into account when trying to segment bone structures in MR images is the non-uniform intensity distribution of the graylevel values. This can be solved by including information regarding the variance of the segmented objects in the evolution function (as proposed by [48]). The PDE describing the hybrid level set model

which combines boundary and region, as well as, statistical information is given in eq. 4.27, with the variance mathematical formulations displayed in eq. 4.28.

$$\frac{\partial \phi}{\partial t} = \delta(\phi)\left[\lambda_2 \frac{(I-\mu_{ext})^2}{\sigma_{ext}^2} - \lambda_1 \frac{(I-\mu_{int})^2}{\sigma_{int}^2} - log\frac{\sigma_{ext}^2}{\sigma_{int}^2} + \beta div\left(g\frac{\nabla\phi}{|\nabla\phi|}\right)\right] \tag{4.27}$$

$$\begin{aligned} \sigma_{int}^2 &= \frac{\int_\Omega (I-\mu_{int})^2 H(\phi) d\Omega}{\int_\Omega H(\phi) d\Omega} \\ \sigma_{ext}^2 &= \frac{\int_\Omega (I-\mu_{ext})^2 (1-H(\phi)) d\Omega}{\int_\Omega (1-H(\phi)) d\Omega} \end{aligned} \tag{4.28}$$

4.3.4 Optimization techniques for level set algorithms

It is very well known that level set segmentation algorithms are computationally expensive and also subject to numerical stability problems. For example, during its evolution, the embedding function ϕ might alter its signed distance function characteristic. This is the reason for which, after a several number of iterations ϕ has to be reinitialized. Practically this step is realised using eq. 4.29 proposed by Sussman et. al. [62], where $\psi(0) = \phi(t)$ and the zero level set of the $\phi(t)$ is the same with the one given by $\psi(t)$, when the converging criteria is achieved. It is also compulsory that the $|\nabla\phi| = 1$, and the property is satisfied by eq. 4.29.

$$\frac{\partial \psi}{\partial t} = sign(\phi(t))(1 - |\nabla\psi|) \tag{4.29}$$

A technique which is capable to reduce the computational costs of the level set methods is called *the narrow band method*. This technique limits the domain for computing the update of the embedding function ϕ. Only a small range of pixels located in the close neighbourhood of the contour are considered. Figure 4.7 represents the thin band which includes the positions considered around the contour. After several iterations, the contour evolves and deforms, approaching the limits of the considered band. In this case the pixel locations for the update of the level set function have to be reinitialized. In practical implementations, choosing a suitable width for the narrow band is an issue, because of the balance between preserving the narrow band and keeping low computational costs. In some cases, the narrow band method can lead to an increase in the propagation speed of the level set. This is possible because the time step is defined based on the highest propagating field in the defined area.

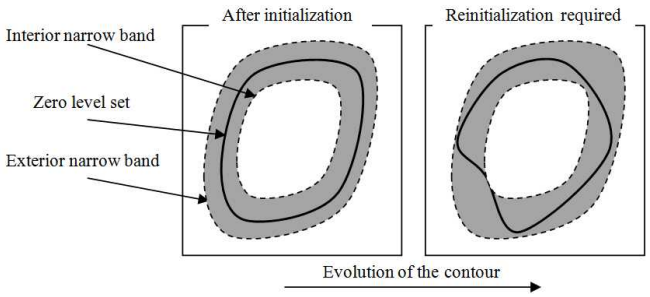

Figure 4.7: Example on how the narrow band is defined in the neighbourhood of the contour and the need for reinitialization after the zero level set evolves

Chapter 5

Results

5.1 Implementation

A 3D segmentation algorithm which integrates the methods described in section 4 has been implemented using two Graphical User Interfaces in MATLAB 2009a. The use of GUIs makes the interaction of the user with the segmentation process much easier. The diagram of the proposed algorithm for extracting the bone structures in MRI datasets is shown in Figure 5.1.

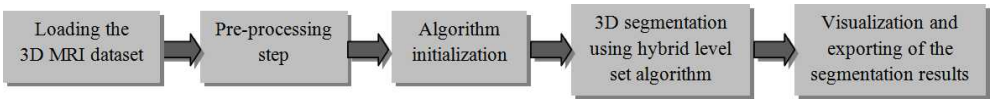

Figure 5.1: Process flow

As shown in Figure 5.1, the first three steps are the loading of the 3D MRI dataset, the pre-processing step and the initialization one. All these stages are accomplished using the GUI presented in Figure 5.2. A brief description is given here for each of the buttons and panels, for a better understanding of the offered capabilities.

- *Load dataset* panel. It includes a browsing button for setting the path of the image volume to be analysed. The user has two options: importing the dataset from a previously saved *MAT-file*, or from a folder containing DICOM files of the scan, by loading and stacking the slice scans into a 3D array. In this stage, also the *metadata* information of the MRI scan is incorporated, which will be used further on during the pre-processing and the exporting steps.

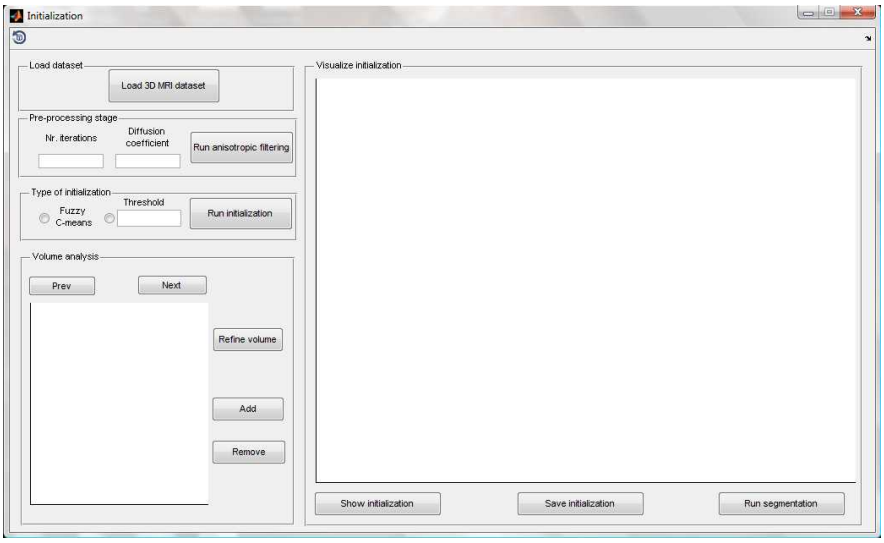

Figure 5.2: Grafical User Interface (GUI) for 3D MRI data loading, pre-processing and initialization

- *Pre-processing step* panel. It implements the noise removal and edge enhancement pre-processing phase using the anisotropic filtering technique developed in section 4.1.2. As explained, two parameters are required: the number of iterations the algorithm has to run and the coefficient which controls the diffusion process.

- *Type of initialization.* In the initialization step the user has to select the starting regions for the bone structures. The initialization for the final segmentation algorithm does not need to be very accurate, but it has to provide only regions inside the structures to be segmented, and not on their borders or outside them. The *K-means* approach (as explained in section 3.3) is based on the assumption that the 3D dataset can be clustered in 3 classes: background, skin and bone. After the K-means clustering technique is run, the initialization 3D volume contains only the pixels considered as bone class. As an alternative, the user can select to threshold the 3D volume. It is known that bone structures usually have higher intensity gray levels than those of the surrounding tissues. Therefore, after visual inspection, the user can select a threshold for binarizing the dataset into bone and non-bone regions. In this case the *single-threshold* introduced in eq. 3.1 is used.

- *Volume analysis* panel. Using the binary initialization 3D volume produced in the previous step, having 1 for a bone voxel and 0 for a non-bone voxel, an algorithm for computing

the connected components (26-connectivity) is used, providing a list of volumes which are possible bone structures. The user has to analyse each volume independently and visually decide if the proposed one can be used as an initialization area or not. The buttons *Prev* and *Next* are used to navigate through the possible bone volumes, and *Add* and *Remove* are employed to include or to exclude the selected amount of voxels in the initialization 3D array. Occasionally, due to the similar graylevel intensity values of the soft tissue (skin, muscle, tendons) and the bone regions, situations can occur in which two bones are connected. For the initialization of the segmentation algorithm only interior areas of bones are needed, excluding any soft tissue. In this case the button *Refine volume* is used, which applies a morphological opening operation (detailed in section 3.6) with a spherical structuring element of a user-selected radius. This results in disconnecting the attached bone structures, keeping only the interior parts of each individual bone. This situation is exemplified in Figure 5.3.

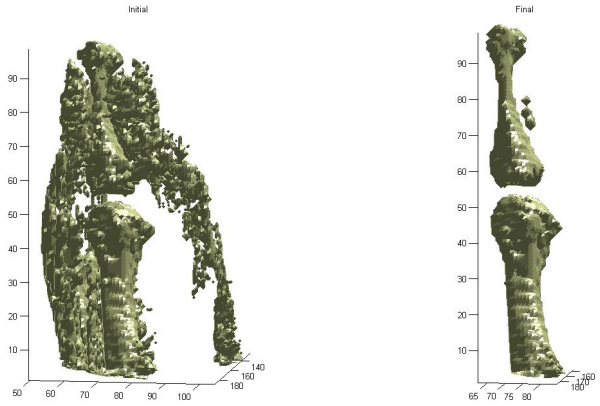

Figure 5.3: Extracting bone structures from volumes including bone and soft tissues using the opening morphological operation

- *Visualize initialization* panel. It is used for the display at any moment of the 3D initialization volume . Its display is updated when the *Show initialization* button is pressed, or a new possible bone volume is analysed using the *Volume analysis* panel. This helps the user to evaluate where the currently studied volume is placed in the 3D initialization array, assisting for an easier decision whether it is a bone structure or not. Finally, when considered, the user can save the 3D initialization using the *Save initialization* button, or can start the segmentation process by using the *Run segmentation* button.

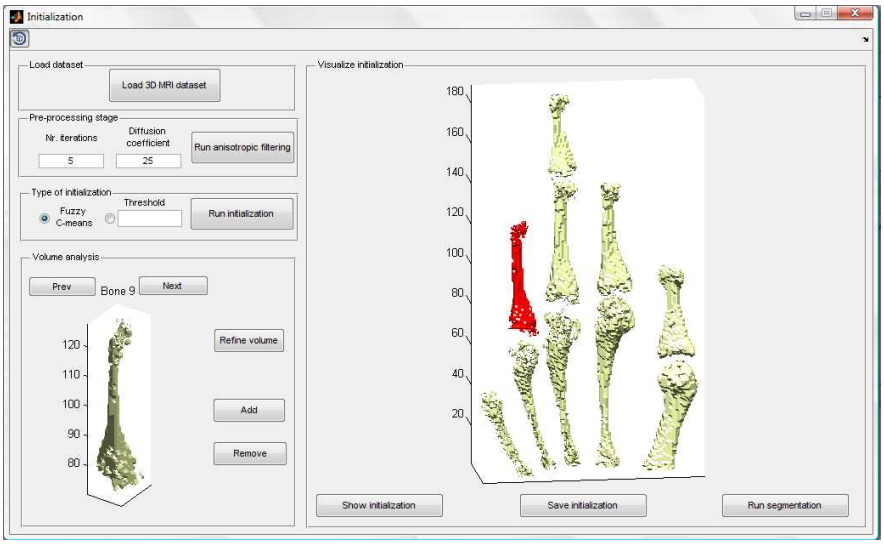

Figure 5.4: Intermediary stage in the initialization process

Figure 5.4 displays an intermediate stage in the initialization process. In the *Preprocessing stage* and *Type of initialization* panels the user can observe the used parameters for the anisotropic diffusion pre-processing step and that the initial volume is computed using the *Fuzzy C-means* clustering procedure detailed in section 4.2. As explained, in the *Volume analysis* panel, the user can navigate through the possible bone volumes, and at a certain step, the current analysed volume (in red) is displayed in the *Visualize initialization* panel. The user can accept it by pressing the *Add* button, and all the validated structures will appear in green in the *Visualize initialization* panel. When the user considers the initialization step is completed, the segmentation process can start.

Bone structures are extracted from the MRI dataset using the hybrid level set algorithm introduced in section 4.3.3. Its applicability is expanded to work on image volumes, by applying it successively on all the slices of the MRI dataset in the 3 orthogonal planes (sagittal, coronal and transversal). At the end, the results of the 2D segmentation steps are merged together, proving the segmented bones. The level set segmentation procedure is detailed in Algorithm 2.

Algorithm 2: Hybrid level set segmentation

1. Load the current 2D slice and the corresponding initialization.
2. Compute the initial embedding function ϕ, using a signed distance map (SDF) introduced in eq. 4.29 and the initial mask which defines the bone regions.
3. Compute the mean values for the interior and exterior regions, as well as the variances, and generate the edge-detector function.
4. Update the embedding function $\phi^{k+1} = \phi^k + \frac{\partial \phi}{\partial t} dt$, using eq. 4.27 for the computation of $\frac{\partial \phi}{\partial t}$.
5. Reinitialize the distance function (SDF) for numerical stability reasons.
6. Repeat steps 3 to 5 until the level set converges (no evolution over several steps).

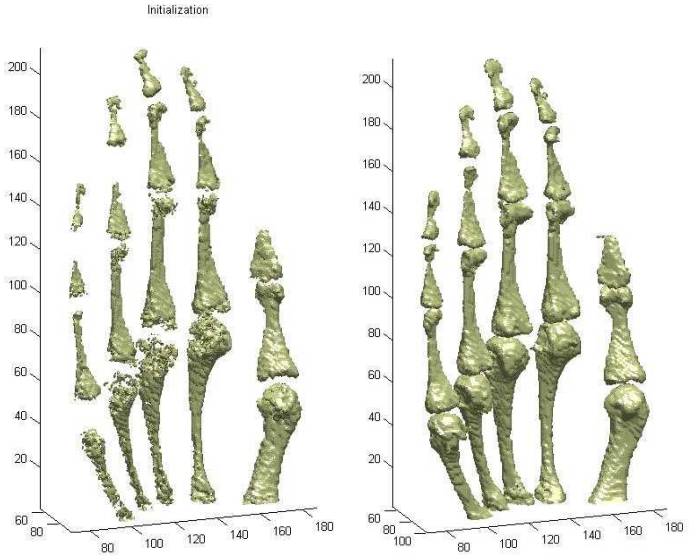

(a) (b)

The result of the 3D hybrid level set segmentation algorithm provides a 3D array, having the same size of the MRI dataset, with values of 1 on voxels classified as part of a bone structure and 0 otherwise. Figure 5.1 displays the resulting segmentation (Figure 5.5(b) having as initialization the volume provided in Figure 5.5(a). It can be concluded that the convergence

of the segmentation algorithm does not depend on the initialization. All the bones are well segmented, even in cases of poor initialization. A more detailed analysis of the performance of the segmentation algorithm is given in section 5.2.

For an easy analysis of the segmentation results another GUI was developed. It's main appearance is shown in Figure 5.5. The user has the option to navigate through all the slices of the 3D MRI volume using a *slider*, the *Next* or *Prev* buttons, or certain slice numbers. Also, one of the three orthogonal planes ((sagittal, coronal and transversal) can be chosen using the *Orientation* option. The performance of the segmentation algorithm can be analysed visually by using the *View initialization* and *View final segmentation buttons* and the evolution of the bone contour can be investigated (as shown in Figure 5.1). The user has the option to export the segmented bone structures in the format of 3D points by pressing the *Export segmentation* button. The procedure for computing the 3D coordinates of a voxel from MRI data is detailed in section 5.3.

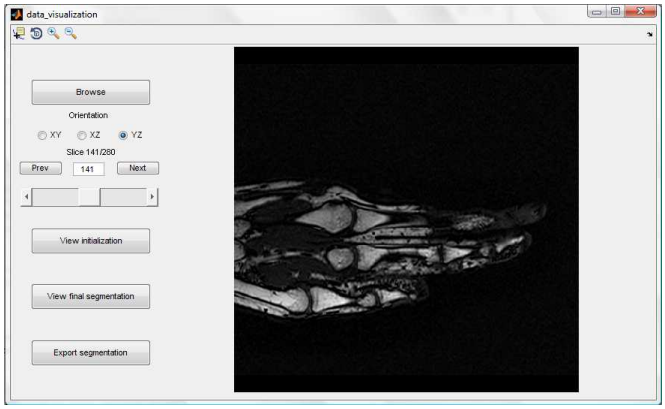

Figure 5.5: Grafical User Interface (GUI) for visualization of the MRI slices, the initial 2D contours and the final segmented bone regions

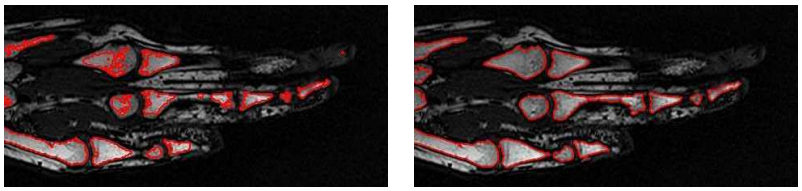

(a) (b)

Figure 5.6: Comparison between the (a) initial contour and (b) the finally segmented bone structures

5.2 Quality measures

The main goal of the segmentation algorithms is to capture as accurate as possible the structures of interest. For the assessment of their performances, the segmentation results are compared with manually segmented ground truth using several quality measures. Further on the chosen evaluation metrics are described, using the notions defined in Figure 5.7.

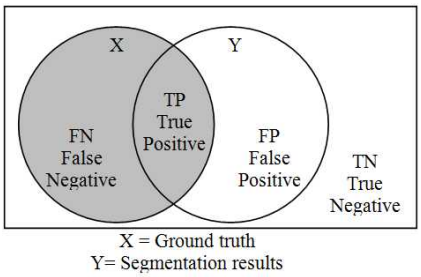

Figure 5.7: Example defining the basic statistical measures using the comparison between segmentation results and the ground truth

The true positive rate, also called *sensitivity*, measures the rate of the accurately recognized positives. On the other hand, *specificity* quantifies the capability of correctly detecting negatives. Ideally, a segmentation algorithm aims for 100% sensitivity, and 100% specificity. Practically, any algorithm would have a minimum prediction error. The mathematical formulations of the two statistical measures are provided in eq. 5.1 and 5.2. Using the defined measures, two other scores can be defined: *the false positive rate* $(1 - specificity)$ and *the false negative rate* $(1 - sensitivity)$.

$$Sensitivity = \frac{TP}{TP + FN} \tag{5.1}$$

$$Specificity = \frac{TN}{FP + TN} \tag{5.2}$$

Accuracy is related to the rate of correct results with respect to the whole domain and *precision* is the percentage of the accurately identified positives with respect to all positive results. Their definitions are confirmed by the eq. 5.3 and 5.4. As well, in the case of these measures, higher percentages refer to higher performances of the assessed segmentation algorithm.

$$Accuracy = \frac{TP + TN}{TP + FP + FN + TN} \tag{5.3}$$

$$Precision = \frac{TP}{TP + FP} \tag{5.4}$$

The similarity between the ground truth and the segmentation results can be also computed using the *Dice coefficient* and is defined as shown in eq. 5.5. A low value for the Dice coefficient would suggest that there is low similarity between the ground truth and the outcome of the segmentation algorithm, while a unity coefficient would denote a perfect segmentation.

$$\begin{aligned} Dice &= \frac{2(X \cap Y)}{X + Y} \\ &= \frac{2TP}{TP + FP + FN} \end{aligned} \tag{5.5}$$

Having described in Figure 5.8 the names of the bones in the human hand, Table 5.1 provides the quality measures of the 3D segmentation algorithm with respect to a manual segmentation considered as the ground truth. The analysis of the segmentation measures in Table 5.1 confirms the good performances of the segmentation algorithm. The high values of the quality measures approve that the algorithm handles a very good segmentation of the bone structures in the MRI datasets.

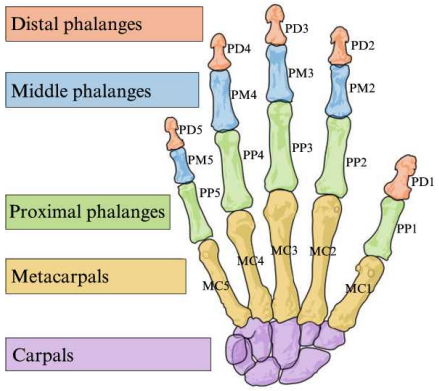

Figure 5.8: Notations of the bones in the human hand

5.3 Exporting the segmentation results

Once the segmentation results are provided, the user has the option to export them, in order to use the bone volumes for the pose estimation step, and later, for the registration stage. For

Bone	Sensitivity	Accuracy	Specificity	Precision	Dice coefficient	Size in pixels
MC1	0.96741	0.99997	1	0.99969	0.99984	57963
PP1	0.9555	0.99998	1	0.99226	0.99611	29708
PD1	0.78592	0.99996	1	0.96714	0.98329	9372
MC2	0.88367	0.99988	1	0.99647	0.99823	57743
PP2	0.91286	0.99995	1	0.99869	0.99935	31323
PM2	0.86748	0.99997	1	0.98444	0.99216	10606
PD2	0.80409	0.99998	1	0.99143	0.9957	4202
MC3	0.92541	0.99993	1	0.99444	0.99721	55557
PP3	0.95677	0.99997	0.99999	0.9909	0.99543	36383
PM3	0.93463	0.99998	1	0.98305	0.99145	13396
PD3	0.92768	0.99999	1	0.97631	0.98802	5742
MC4	0.94166	0.99994	0.99998	0.96383	0.98158	37930
PP4	0.96279	0.99998	1	0.99302	0.9965	25643
PM4	0.82595	0.99997	0.99999	0.96077	0.97999	8999
PD4	0.94122	1	1	0.99052	0.99524	4219
MC5	0.99658	0.99995	0.99996	0.911	0.95343	31685
PP5	0.99772	0.99997	0.99997	0.90574	0.95054	18322
PM5	0.979	0.99999	0.99999	0.86632	0.92837	6134
PD5	1	1	1	0.88937	0.94144	2784
all	0.93195	0.99935	0.99985	0.97824	0.989	447832

Table 5.1: Quality measures for the 3D bone segmentation

an accurate estimation of the position of the bones and of the motion of a certain bone volume from one posture to another, the clouds of points have to be represented with respect to the same reference system. This can be achieved using the information provided by the DICOM format in the metadata file of the MRI dataset.

The Digital Imaging and Communications in Medicine (DICOM) standard was developed by NEMA (National Electrical Manufacturers Association) with the scope of an easy and efficient medical imaging storage and transmission. A DICOM file encloses two main parts: a header and the image data. The header contains details related to the patient, the type of the scan and the used parameters and the geometry of the medical image dataset. The DICOM format uses a right handed coordinate system (LPH) and helps relate the medical image dataset with a 3D fixed reference system. In order to compute the 3D coordinates of a voxel in the medical image volume, the following fields provided in the header of the DICOM file are needed:

- *ImagePositionPatient (IPP)* - the 3D coordinates (in millimetres) of the pixel placed on the top left location of the studied slice.

- *PixelSpacing (PS)* - a vector of 2 variables providing the distance in millimetres between

the centers of two neighbouring pixels: the first value is the distance between two rows (vertical spacing) and the second one provides the gap between two columns (horizontal spacing).

- *ImageOrientationPatient (IOP)* - providing two unit vectors stating the directions cosines of the rows and colums.
- *Height* - the number of rows.
- *Width* - the number of colums.

Having the aforementioned notions described in Figure 5.9(a), and the configuration illustrated in Figure 5.9(b), the 3D position of the pixel of interest (denoted by POS) with respect to the LPH reference system is given by equation 5.6, where N_ROW and N_COL are the row and the column indexes of the pixel of interest. Using this mathematical formulation, every voxel in the dataset is exported with respect to the 3D LPH coordonate system.

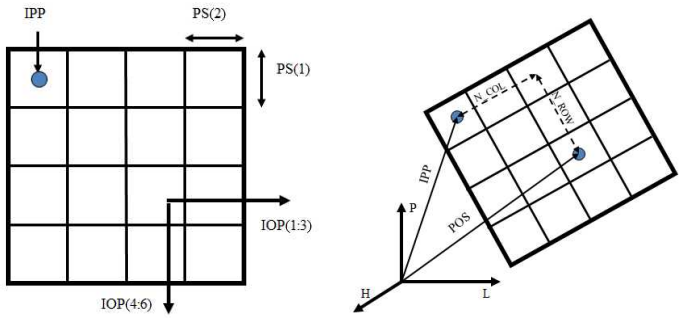

(a) (b)

Figure 5.9: Computing 3D coordinates using the geometry information provided by the header of the DICOM file

$$POS = IPP + N\_COL * IOP(1:3) * PS(2) + N\_ROW * IOP(4:6) * PS(1) \tag{5.6}$$

Bibliography

[1] Hand. Britannica Encyclopaedia. http://www.britannica.com/EBchecked/media/101313/Bones-of-the-hand-showing-the-carpal-bones-metacarpal-bones, 2011.

[2] B. Dogdas A, D. Shattuck B, and R. M. Leahy C. Segmentation of skull in 3d human mr images using mathematical morphology.

[3] G B Aboutanos, J Nikanne, N Watkins, and B M Dawan. Model creation and deformation for the automatic segmentation of the brain in mr images. *IEEE Transactions on Biomedical Engineering*, 46(11):1346–1356, 1999.

[4] S. Aja Fernandez, C. Alberola Lopez, and C.F. Westin. Noise and signal estimation in magnitude mri and rician distributed images: A lmmse approach. 17(8):1383–1398, August 2008.

[5] Santiago Aja-Fernndez, Antonio Tristn-Vega, and Carlos Alberola-Lpez. Noise estimation in single- and multiple-coil magnetic resonance data based on statistical models. *Magnetic Resonance Imaging*, 27(10):1397–1409, 2009.

[6] N C Andreasen, R Rajarethinam, T Cizadlo, S Arndt, 2nd Swayze V W, L A Flashman, D S O'Leary, J C Ehrhardt, and W T Yuh. Automatic atlas-based volume estimation of human brain regions from MR images. *Journal of Computer Assisted Tomography*, 20(1):98–106, February 1996. PMID: 8576490.

[7] M. Stella Atkins and Blair T. Mackiewich. Handbook of medical imaging. chapter Fully automated hybrid segmentation of the brain, pages 171–183. Academic Press, Inc., Orlando, FL, USA, 2000.

[8] K T Bae, M L Giger, C T Chen, and Jr Kahn C E. Automatic segmentation of liver structure in CT images. *Medical Physics*, 20(1):71–78, February 1993. PMID: 8455515.

[9] J C Bezdek, L O Hall, and L P Clarke. Review of MR image segmentation techniques using pattern recognition. *Medical Physics*, 20(4):1033–1048, August 1993. PMID: 8413011.

[10] A Bosnjak, G Montilla, R Villegas, and I Jara. 3d segmentation with an application of level set-method using mri volumes for image guided surgery. *Conference Proceedings of the International Conference of IEEE Engineering in Medicine and Biology Society*, 2007:5263–5266.

[11] M.E. Brummer, R.M. Mersereau, R.L. Eisner, and R.R.J. Lewine. Automatic detection of brain contours in MRI data sets. *IEEE Transactions on Medical Imaging*, 12(2):153–166, 1993.

[12] Andrew J. Burghardt, Galateia J. Kazakia, and Sharmila Majumdar. A local adaptive threshold strategy for high resolution peripheral quantitative computed tomography of trabecular bone. *Annals of Biomedical Engineering*, 35(10):1678–1686, 2007.

[13] Vicent Caselles, Ron Kimmel, and Guillermo Sapiro. Geodesic active contours. *International Journal of Computer Vision*, 22:61–79, 1995.

[14] Tony F. Chan and Luminita A. Vese. Active contours without edges. *IEEE Transactions on Image Processing*, 10:266–277, 2001.

[15] Songcan Chen and Daoqiang Zhang. Robust image segmentation using FCM with spatial constraints based on new kernel-induced distance measure. *Systems, Man, and Cybernetics, Part B: Cybernetics, IEEE Transactions on*, 34(4):1907–1916, August 2004.

[16] Gary E. Christensen, Sarang C. Joshi, Michael I. Miller, and Senior Member. Volumetric transformation of brain anatomy. *IEEE Transactions on Medical Imaging*, 16:864–877, 1997.

[17] G.B. Coleman and H.C. Andrews. Image segmentation by clustering. *Proceedings of the IEEE*, 67(5):773–785, 1979.

[18] Louis Collins, CJ Holmes, TM Peters, and AC Evans. Automatic 3-D model-based neuroanatomical segmentation. *Human Brain Mapping*, 3(3):190–208, 1995.

[19] Christos Davatzikos and Christos Davatzikos. Spatial normalization of 3d brain images using deformable models. *Journal of Computer Assisted Tomography*, 20:656–665, 1996.

[20] David L. Donoho. De-noising by soft-thresholding. *IEEE Transactions on Information Theory*, 41:613–627, 1995.

[21] M. Droske, B. Meyer, M. Rumpf, and K. Schaller. An adaptive level set method for medical image segmentation, 2001.

[22] Aly A. Farag, Ph. D, Hossam Hassan, Robert Falk, Stephen G. Hushek, and Ph. D. 3d volume segmentation of mra data sets using level sets.

[23] Y Ge, J M Fitzpatrick, B M Dawant, J Bao, R M Kessler, and R A Margolin. Accurate localization of cortical convolutions in MR brain images. *IEEE Transactions on Medical Imaging*, 15(4):418–428, 1996. PMID: 18215924.

[24] Guido Gerig, Olaf Kubler, Ron Kikinis, and Ferenc A. Jolesz. Nonlinear anisotropic filtering of mri data, 1992.

[25] A F Goldszal, C Davatzikos, D L Pham, M X Yan, R N Bryan, and S M Resnick. An image-processing system for qualitative and quantitative volumetric analysis of brain images. *Journal of Computer Assisted Tomography*, 22(5):827–837, October 1998. PMID: 9754125.

[26] V. Grau, A. U. J. Mewes, M. Alcaniz, R. Kikinis, and S. K. Warfield. Improved watershed transform for medical image segmentation using prior information. *Medical Imaging, IEEE Transactions on*, 23(4):447–458, April 2004.

[27] Robert M. Haralick and Linda G. Shapiro. Image segmentation techniques. *Computer Vision, Graphics, and Image Processing*, 29(1):100–132, January 1985.

[28] K Held, E Rota Kops, B J Krause, 3rd Wells W M, R Kikinis, and H W Mller-Grtner. Markov random field segmentation of brain MR images. *IEEE Transactions on Medical Imaging*, 16(6):878–886, December 1997. PMID: 9533587.

[29] Sijbers J., Poot D. H. J., den Dekker A. J., and Pintjens W. Automatic estimation of the noise variance from the histogram of a magnetic resonance image. *Physics in Medicine and Biology*, 52(5):1335–1348, February 2007.

[30] Y. Jiang. X-ray bone fracture subtraction using geodesic active contour and mathematical morphology operations. In *CARS*, pages 226–231, 2003.

[31] Michael Kass, Andrew Witkin, and Demetri Terzopoulos. Snakes: Active contour models. *INTERNATIONAL JOURNAL OF COMPUTER VISION*, 1(4):321–331, 1988.

[32] Rasoul Khayati, Mansur Vafadust, Farzad Towhidkhah, and Massood Nabavi. Fully automatic segmentation of multiple sclerosis lesions in brain mr flair images using adaptive mixtures method and markov random field model. *Comput. Biol. Med.*, 38:379–390, March 2008.

[33] J. Kittler, J. Illingworth, and J. Fglein. Threshold selection based on a simple image statistic. *Computer Vision, Graphics, and Image Processing*, 30(2):125–147, May 1985.

[34] G Kom, A Tiedeu, and M Kom. Automated detection of masses in mammograms by local adaptive thresholding. *Computers in Biology and Medicine*, 37(1):37–48, 2007.

[35] Jakub Kratky and Jan Kybic. Three-dimensional segmentation of bones from ct and mri using fast level sets. *Proceedings of SPIE*, 6914(1):691447–691447–10, 2008.

[36] T. Lei and W. Sewchand. Statistical approach to x-ray CT imaging and its applications in image analysis. i. statistical analysis of x-ray CT imaging. *Medical Imaging, IEEE Transactions on*, 11(1):53–61, March 1992.

[37] Chunming Li, Rui Huang, Zhaohua Ding, Chris Gatenby, Dimitris Metaxas, and John Gore. A variational level set approach to segmentation and bias correction of images with intensity inhomogeneity. In *Proceedings of the 11th International Conference on Medical Image Computing and Computer-Assisted Intervention, Part II*, MICCAI '08, pages 1083–1091, Berlin, Heidelberg, 2008. Springer-Verlag.

[38] H Li, R Deklerck, B De Cuyper, A Hermanus, E Nyssen, and J Cornelis. Object recognition in brain CT-scans: knowledge-based fusion of data from multiple feature extractors. *IEEE Transactions on Medical Imaging*, 14(2):212–229, 1995. PMID: 18215825.

[39] S. Z. Li. Markov random field models in computer vision. In *Proceedings of the third European conference on Computer Vision (Vol. II)*, pages 361–370, Secaucus, NJ, USA, 1994. Springer-Verlag New York, Inc.

[40] Zhengrong Liang, J.R. MacFall, and D.P. Harrington. Parameter estimation and tissue segmentation from multispectral MR images. *IEEE Transactions on Medical Imaging*, 13(3):441–449, September 1994.

[41] Liana M. Lorigo, Olivier D. Faugeras, W. Eric L. Grimson, Renaud Keriven, and Ron Kikinis. Segmentation of bone in clinical knee mri using texture-based geodesic active contours. In *Proceedings of the First International Conference on Medical Image Computing and Computer-Assisted Intervention*, MICCAI '98, pages 1195–1204, London, UK, 1998. Springer-Verlag.

[42] J.B.Antoine Maintz and Max A. Viergever. A survey of medical image registration. *Medical Image Analysis*, 2(1):1–36, March 1998.

[43] Jean-François Mangin, Vincent Frouin, Isabelle Bloch, Jean Régis, and Jaime López-Krahe. From 3d magnetic resonance images to structural representations of the cortex topography using topology preserving deformations. *J. Math. Imaging Vis.*, 5:297–318, December 1995.

[44] I N Manousakas, P E Undrill, G G Cameron, and T W Redpath. Split-and-merge segmentation of magnetic resonance medical images: performance evaluation and extension to three dimensions. *Computers and Biomedical Research, an International Journal*, 31(6):393–412, December 1998. PMID: 9843626.

[45] D. Nadadur and R. M Haralick. Recursive binary dilation and erosion using digital line structuring elements in arbitrary orientations. *Image Processing, IEEE Transactions on*, 9(5):749–759, May 2000.

[46] Laurent Najman and Michel Schmitt. Geodesic saliency of watershed contours and hierarchical segmentation. *IEEE Transactions on Pattern Analysis and Machine Intelligence*, 18:1163–1173, 1996.

[47] Robert D. Nowak. Wavelet-based rician noise removal for magnetic resonance imaging, 1998.

[48] Stanley Osher and Nikos Paragios. *Geometric Level Set Methods in Imaging,Vision,and Graphics*. Springer-Verlag New York, Inc., Secaucus, NJ, USA, 2003.

[49] Stanley Osher and James A. Sethian. Fronts propagating with curvature dependent speed: Algorithms based on hamilton-jacobi formulations. *JOURNAL OF COMPUTATIONAL PHYSICS*, 79(1):12–49, 1988.

[50] P. Perona and J. Malik. Scale-space and edge detection using anisotropic diffusion. *IEEE Trans. Pattern Anal. Mach. Intell.*, 12:629–639, July 1990.

[51] D. L. Pham, C. Xu, and J. L. Prince. A survey of current methods in medical image segmentation. In *Annual Review of Biomedical Engineering*, volume 2, pages 315–338. 2000.

[52] Dzung L. Pham and Jerry L. Prince. An adaptive fuzzy c-means algorithm for image segmentation in the presence of intensity inhomogeneities. *Pattern Recognition Letters*, 20:57–68, 1998.

[53] Jerry L Prince, Azar P Dagher, Chenyang Xu, Dzung Pham, and Dzung Pham. An automated technique for statistical characterization of brain tissues in magnetic resonance imaging. 1996.

[54] G. N. Harikrishna Rai and T. R. Gopalakrishnan Nair. Gradient based seeded region grow method for ct angiographic image segmentation. *CoRR*, abs/1001.3735, 2010.

[55] P. K Sahoo, S. Soltani, A. K. C Wong, and Y. C Chen. A survey of thresholding techniques. *Computer Vision, Graphics, and Image Processing*, 41:233260, February 1988. ACM ID: 46079.

[56] Nong Sang, Heng Li, Weixue Peng, and Tianxu Zhang. Knowledge-based adaptive thresholding segmentation of digital subtraction angiography images. *Image Vision Comput.*, 25:1263–1270, August 2007.

[57] A. Sarti, C. Corsi, E. Mazzini, and C. Lamberti. Maximum likelihood segmentation of ultrasound images with rayleigh distribution. *IEEE Transactions on Ultrasonics, Ferroelectrics and Frequency Control*, 52(6):947–960, 2005.

[58] Jean Serra. *Image Analysis and Mathematical Morphology*. Academic Press, Inc., Orlando, FL, USA, 1983.

[59] Linda Shapiro, George Stockman, Linda Shapiro, and George Stockman. *Computer Vision*. Prentice Hall, January 2001.

[60] Georg Stillfried and Patrick van der Smagt. Movement model of a human hand based on magnetic resonance imaging (mri). In *1st International Conference on Applied Bionics and Biomechanics (ICABB) 2010*, October 2010.

[61] Matús Straka, Alexandra La Cruz, Arnold Köchl, Milos Srámek, Meister Eduard Gröller, and Dominik Fleischmann. 3d watershed transform combined with a probabilistic atlas for medical image segmentation, 2003.

[62] Mark Sussman, Peter Smereka, and Stanley Osher. A level set approach for computing solutions to incompressible two-phase flow. *J. Comput. Phys.*, 114:146–159, September 1994.

[63] P M Thompson and A W Toga. Detection, visualization and animation of abnormal anatomic structure with a deformable probabilistic brain atlas based on random vector field transformations. *Medical Image Analysis*, 1(4):271–294, September 1997. PMID: 9873911.

[64] H. Tian, T. Srikanthan, and K. Vijayan Asari. Automatic segmentation algorithm for the extraction of lumen region and boundary from endoscopic images. *Medical & Biological Engineering & Computing*, 39(1):8–14, 2001.

[65] Jayaram K. Udupa and Supun Samarasekera. Fuzzy connectedness and object definition: Theory, algorithms, and applications in image segmentation. *Graphical Models and Image Processing*, 58(3):246–261, May 1996.

[66] Henri A. Vrooman. kNN-based multi-spectral MRI brain tissue classification: manual training versus automated atlas-based training. In *Proceedings of SPIE*, pages 61443L–61443L–9, San Diego, CA, USA, 2006.

[67] Jianzhong Wang, Jun Kong, Yinghua Lu, Miao Qi, and Baoxue Zhang. A modified FCM algorithm for MRI brain image segmentation using both local and non-local spatial constraints. *Computerized Medical Imaging and Graphics: The Official Journal of the Computerized Medical Imaging Society*, 32(8):685–698, December 2008. PMID: 18818051.

[68] W M Wells, W L Grimson, R Kikinis, and F A Jolesz. Adaptive segmentation of MRI data. *IEEE Transactions on Medical Imaging*, 15(4):429–442, 1996. PMID: 18215925.

[69] C.-F. Westin, L. M. Lorigo, O. D. Faugeras, W. E. L. Grimson, S. Dawson, A. Norbash, and R. Kikinis. Segmentation by adaptive geodesic active contours. In A. M. DiGioia and S. Delp, editors, *Proceedings of MICCAI 2000, Third International Conference on Medical Image Computing and Computer-Assisted Intervention*, pages 266–275, Pittsburgh, October 11-14 2000.

[70] Andrew P. Witkin. Scale-space filtering. In *IJCAI*, pages 1019–1022, 1983.

[71] Chenyang Xu and Jerry L. Prince. Snakes, shapes, and gradient vector flow. *IEEE TRANSACTIONS ON IMAGE PROCESSING*, 7(3):359–369, 1998.

[72] Miin-Shen Yang and Chen-Feng Su. On parameter estimation for normal mixtures based on fuzzy clustering algorithms. *Fuzzy Sets Syst.*, 68:13–28, November 1994.

[73] L.A Zadeh. Fuzzy sets as a basis for a theory of possibility. *Fuzzy Sets and Systems*, 1(1):3–28, January 1978.

[74] J. Zhang, C.-H. Yan, C.-K. Chui, and S.-H. Ong. Fast segmentation of bone in CT images using 3D adaptive thresholding. *Computers in Biology and Medicine*, 40(2):231–236, 2010.

[75] Yan Zhang, Bogdan J. Matuszewski, Lik-Kwan Shark, and Christopher J. Moore. Medical image segmentation using new hybrid level-set method. In *Proceedings of the 2008 Fifth International Conference BioMedical Visualization: Information Visualization in Medical and Biomedical Informatics*, pages 71–76, Washington, DC, USA, 2008. IEEE Computer Society.

[76] A P Zijdenbos and B M Dawant. Brain segmentation and white matter lesion detection in MR images. *Critical Reviews in Biomedical Engineering*, 22(5-6):401–465, 1994. PMID: 8631195.